1-1-2015

An Experimental Investigation of Dual-Injection Strategies on Diesel-Methane Dual-Fuel Low Temperature Combustion in a Single Cylinder Research Engine

Aamir Sohail

An experimental investigation of dual-injection strategies on diesel-methane dual-fuel low temperature combustion in a Single Cylinder Research Engine

By

Aamir Sohail

A Thesis
Submitted to the Faculty of
Mississippi State University
in Partial Fulfillment of the Requirements
for the Degree of Master of Science
in Mechanical Engineering
in the Department of Mechanical Engineering

Mississippi State, Mississippi

August 2015

An experimental investigation of dual-injection strategies on diesel-methane dual-fuel low temperature combustion in a Single Cylinder Research Engine

By

Aamir Sohail

Approved:

_____

Kalyan K. Srinivasan
(Major Professor)

_____

Sundar R. Krishnan
(Co-Major Professor)

_____

William T. French
(Committee Member)

_____

Mark F. Horstemeyer
(Graduate Coordinator)

_____

Jason M. Keith
Interim Dean
Bagley College of Engineering

Name: Aamir Sohail

Date of Degree: August 14, 2015

Institution: Mississippi State University

Major Field: Mechanical Engineering

Major Professor: Kalyan K. Srinivasan

Title of Study: An experimental investigation of dual-injection strategies on diesel-methane dual-fuel low temperature combustion in a Single Cylinder Research Engine

Pages in Study: 84

Candidate for Degree of Master of Science

The present manuscript discusses the performance and emission benefits due to two diesel injections in diesel-ignited methane dual fuel Low Temperature Combustion (LTC). A Single Cylinder Research Engine (SCRE) adapted for diesel-ignited methane dual fuelling was operated at 1500 rev/min and 5 bar BMEP with 1.5 bar intake manifold pressure. The first injection was fixed at 310 CAD. A 2nd injection sweep timing was performed to determine the best 2nd injection timing (as 375 CAD) at a fixed Percentage Energy Substitution (PES 75%). The motivation to use a second late injection ATDC was to oxidize Unburnt Hydrocarbons (HC) generated from the dual fuel combustion of first injection. Finally, an injection pressure sweep (550-1300 bar) helped achieve simultaneous reduction of HC (56%) and CO (43%) emissions accompanied with increased IFCE (10%) and combustion efficiency (12%) w.r.t. the baseline single injection (at 310 CAD) of dual fuel LTC.

DEDICATION

This manuscript is a dedicated to my beloved parents who nurtured me, siblings for being sources of constant inspiration, friends who believed in me and teachers who taught me to jumble up words to make these sentences.

I would like to quote a section of a poem which has kept me raring and strive for that extra bit:

The woods are lovely, dark and deep,
But I have promises to keep,
And miles to go before I sleep,
And miles to go before I sleep.

- *Robert Frost*
Poem: *Stopping by Woods on a Snowy Evening*
Book: *The Poetry of Robert Frost*
ISBN-13: 978-0030491269

ACKNOWLEDGEMENTS

I offer my humble gratitude to my major advisor and mentor-in-chief, Dr. Kalyan K. Srinivasan and co-major advisor Dr. Sundar R. Krishnan. I am thankful to them on many accounts, foremost of all for providing me with an invaluable opportunity to work with them in the Advanced Combustion Engines (ACE) lab at Mississippi State University. I am deeply impressed not just with their knowledge about engines research but their temperament towards society, cultures, environment and life as a whole. It is their keenness and curiosity to learn that I tried to instill within me while my tenure as a graduate student at MSU. Their teachings shall continue shaping me for the rest of my life.

I am indebted to Dr. William T. French for agreeing to serve on my graduate committee. His timely advice and words of inspiration and were valuable towards realizing this degree. I express my humble gratitude to the Bagley College of Engineering, Mississippi State University for providing the financial support to carry out this research and the Center for Advanced Vehicular Systems (CAVS) at Mississippi State University for the facilities support. I am obliged to the Mechanical Engineering department secretaries Ms. Delia Nuckolls, Ms. Linda Schubert and Ms. Dianne for providing me a warm kinship and ensuring the timely arrival of my paychecks from my research assistantship. I am especially appreciative of Ms. Debi Brewington,

administrative assistant at CAVS for her words of encouragement and amusing conversations.

I am thankful to my lab colleagues Mostafa Shameem Raihan, Scott Guerry, Kyle Hodges, Taylor Bohach, Navid Zanganeh, David Dickerson, Kendyl Patridge, Prabhat Jha and Hamidreza Mahabadipour for their assistance and unaccountable support while conducting this research. In Shameem, I found an excellent mentor and a friend. If not for his ingenious timely rescues, I would have found myself stuck on many occasions. I am grateful to Kyle and Taylor for grooming me to the different instruments in the lab, I was unsure how to work with. I wish them all the best for their PhD and Master's studies, respectively. I owe a lot to ex-lab mate Umang Dwivedi for his guidance while my transition from India to USA and constant stimulation regarding my studies and research. I am grateful to Jake Kizer from Altech E.S.A. for helping me troubleshoot the emissions bench.

I owe gratitude to Anay Ismail, Suwaira Iqbal, Nitin, Sanchit & Marina for making my stay in Starkville a pleasant experience. I am thankful to my badminton allies Dr. Thu Dinh, Prateek Jolly, Anuraj Theradiyil, Rahul Gubbala, Kalyan Kota and others for those great games which helped me ease out my nerves. I gratefully acknowledge the hospitality of the Indian Student Association for seldom letting me realize that I was half a globe away from *home*. I appreciate the warm and accommodating people of Starkville, Mississippi for the indispensable role they continue to play in my personal and professional growth.

I thank Dhawal Kushwaha and Bahubali Jain, my undergraduate colleagues who garnered passion in me about engines. I am grateful to have found awesome bunch of supportive friends in Zergham Naqvi, KP Shreekant and Aquib Khan from Indore, India.

I pay my tribute to my parents Mr. Masih Alam and Mrs. Nasima Begum for giving me the freedom of choice & backing me up through the engulfing lows in my career and my siblings for being phenomenal sources of inspiration. It is to them that I owe every bit of what I have achieved so far.

TABLE OF CONTENTS

LIST OF TABLES

LIST OF FIGURES

NOMENCLATURE

AHRR	Apparent Heat Release Rate
ALPING	Advanced Low Pilot Injection Natural Gas
ATDC	After Top Dead Center
BDC	Bottom Dead Center
BMEP	Net Brake Mean Effective Pressure
CA 10-90	Crank Angle duration between locations of 10% and 90% cumulative heat release
CA5	Crank Angle at which 5% of cumulative heat release occurs
CA50	Crank Angle at which 50% of cumulative heat release occurs
CAD	Crank Angle Degree
CARB	California Air Resources Board
CI	Compression Ignition
CO	Carbon monoxide
COV IMEP	Coefficient of Variation of IMEP
EEPS	Engine Exhaust Particle Sizer
EGR	Exhaust Gas Recirculation
EOTC	Engine Oil Temperature Conditioner
EPA	Environmental Protection Agency
EVC	Exhaust Valve Close

EVO	Exhaust Valve Open
EWTC	Engine Water Temperature Conditioner
FCE	Fuel Conversion Efficiency
FSN	Filter Smoke Number
HC	Unburned Hydrocarbons
HCCI	Homogenous Charge Compression Ignition
ID	Ignition delay
IFCE	Net Indicated Fuel Conversion Efficiency
IMEP	Net Indicated Mean Effective Pressure
ISCO	Net Indicated Specific Carbon Monoxide
ISHC	Net Indicated Specific Hydrocarbons
ISNOx	Net Indicated Specific Oxides of Nitrogen
IVC	Intake Valve Close
IVO	Intake Valve Open
kg/kmol	kilograms per kilo mole
LHV	Lower Heating Value
LTHR	Low Temperature Heat Release
MJ/kg	Mega Joules per kilogram
MPRR	Maximum Pressure Rise Rate
ms	milliseconds
NOx	Nitrogen Oxides
OP	Operating Point
O_2	Oxygen

PCCI	Premixed Charge Compression Ignition
PES	Percent Energy Substitution
PM	Particulate Matter
ppm	parts per million
QLHV	Mass-averaged Lower Heating Value (kJ/kg)
RCCI	Reactivity Controlled Compression Ignition
SADI	Stand-Alone Diesel Injector
SCRE	Single Cylinder Research Engine
SI	Spark Ignition
SOC	Start Of Combustion
SOI	Start Of Injection
TDC	Top Dead Center
US EPA	United States Environmental Protection Agency
v/s	Versus
w.r.t.	with respect to

Subscripts:

a	air
d	diesel
f	fuel
g	gaseous methane fuel
st	stoichiometric

CHAPTER I

INTRODUCTION AND REVIEW OF EXISTING LITERATURE

1.1 Fundamentals of Diesel Engine Combustion

Combustion, especially as it occurs in Internal Combustion Engines (ICE) has been a field of much research and development. Considering more than 100 years of their existence, the working principle of ICEs have remained essentially the same, wherein an ignitable fluid called a fuel is used to control-detonate and pressurize a combustion chamber resulting in the downward motion of a piston coupled with a crankshaft to provide mechanical power output. The two types of engines (mainly based on their fuels) most abundantly used are Gasoline (also referred to as Spark Ignition, SI) and Diesel (also referred to as Compression Ignition, CI) engines. Owing to their superior fuel efficiency at higher load conditions, CI engines have an edge over SI engines.

A certain and obnoxious compromise accompanying CI engines is the formation of Nitrogenous Oxides (NOx) and soot (also referred to as Particulate Matter, PM). Moreover, there is a trade-off between the two emissions, i.e. one is decreased for the expense of the other. It is imperative to know how this trade-off comes into light. The most universally accepted conceptual model of the diesel spray and its combustion was provided by Dec, 1997. A schematic of Dec's model is depicted in Figure 1.1. The professed model was formulated using chemiluminescence and laser sheet imaging

techniques in an optically accessible combustion chamber of a production engine. According to the model, the diesel spray upon being atomized into the combustion chamber, is subjected to spatially varying fuel-air mixtures (equivalence ratios). The start of combustion occurs near the depicted fuel-rich premixed region with equivalence ratios 2-4. Further into the combustion regime, a diffusion flame envelops the spray jet from the outward periphery where the equivalence ratio is near to stoichiometric and consequently the flame temperatures are the highest. The model reveals that soot starts its formation near the fuel-rich premixed region while NOx initiates its formation in the relatively hotter outward peripheral regions. The higher flame temperatures oxidize the soot thereby reducing its emissions, meanwhile also leading to higher NOx formation, thus establishing the NOx-soot trade-off.

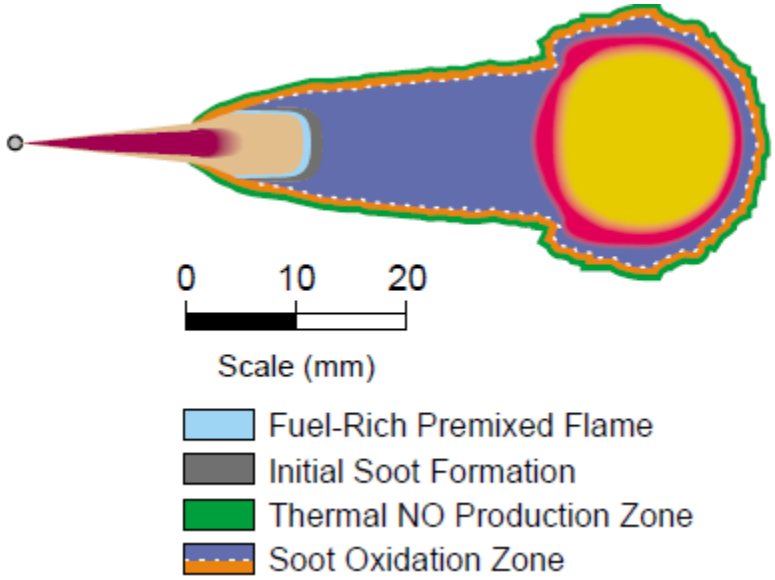

Figure 1.1 Conceptual model of diesel spray combustion.

Adapted from Dec, 1997

Emission levels of these engine-effluents are regulated and made increasingly stringent by the governmental regulatory bodies. The U.S. Environmental Protection Agency (US EPA) is such a body which restricts the brake-specific NOx and soot emissions of heavy-duty CI engines to 0.027 and 0.013 g/kW-hr respectively (Diesel Net, 2015). Quite a few after-treatment devices have been developed and made available commercially to achieve this target. CI engines normally operate lean of stoichiometric conditions, rendering more oxygen in the exhaust to prevent the use of 3-Way Catalysts for converting NOx into N_2 and O_2; however, the deployment of Selective Catalytic Reduction (SCR) is successful at reducing NOx, but requires injection of urea which is an additional economic burden which is estimated at 1% of fuel consumed per g/kW-hr of NOx reduction (Johnson 2011). Additionally, the Diesel Particulate Filters (DPFs) have been successful in reducing soot emissions, but only at the expense of fuel efficiency as they employ a periodic injection of rich air-fuel mixture of diesel to oxidize the accumulated soot particles by raising the temperature in the DPF which activates the catalyst.

The DPFs are useful for the larger sized particles. Dockery (1994) showed that particles finer than 50 μm lead to severe health problems. Advanced combustion strategies (as described under 1.3 and 1.4 of this chapter) lead to an undesired effect of reducing the exhaust particle sizes to nanoscales. Such nanoparticles tend to skip the DPF and go out in the atmosphere, creating more environmental and health hazards. A schematic of the harmful effects of finer exhaust particles (Particulates health risks 2015) has been shown in Fig. 1.2.

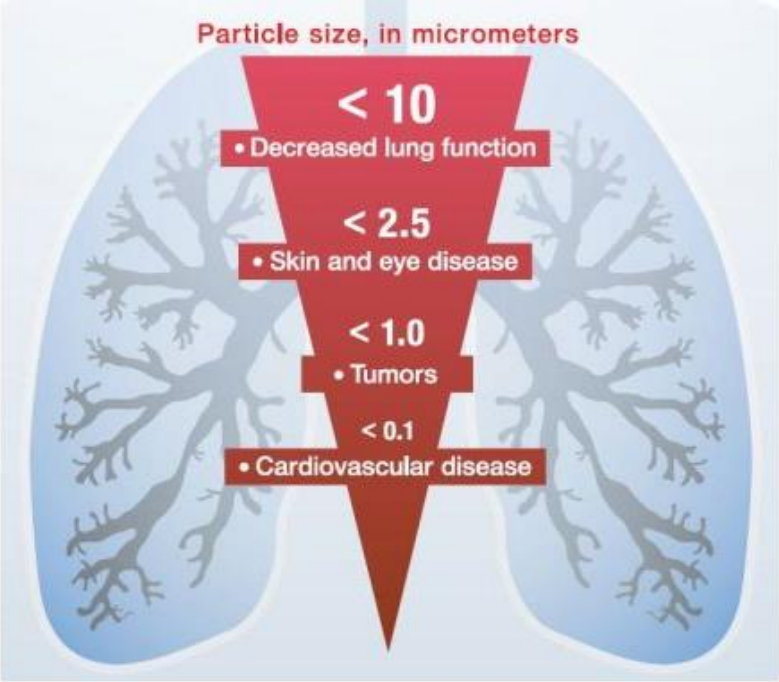

Figure 1.2 Harmful effects of finer exhaust particles.

Adapted from http://www.tesa-clean-air.com/eng/fine_dust_particles

1.2 Viability of Methane as an alternate fuel

Experimentalists have tried propane (Ma et al. 2007, Polk et al. 2013); dimethyl ether (Chen et al. 2000, Sorenson et al. 2001); biodiesel blends (Lu et al. 2008., Northrop et al. 2009). Methane is a popular choice of alternate fuel among researchers owing to its economic viability, simpler molecular structure (as compared to diesel, propane or oxygenated blends) and lower cetane number. Methane is the primary constituent of Natural Gas with up to 98% of methane content. As far as the United States is concerned, vast reserves of available natural gas and the recent evolution of *fracking* as an effective process of natural gas extraction has brought about confidence in selecting methane as a viable alternative fuel. Natural gas extraction has recorded 30% increase in the last 5 years and 12% increase from January 2014-January 2015 alone (U. S. Energy

Information Administration 2015). It stands second as the most used fuel after petroleum representing about 30% of the total usage as of November 2014 (U. S. Energy Information Administration 2015). Thus methane projects a promising future as an alternative to diesel.

The following table enlists the composition of the methane used in this study:

Table 1.1 Methane composition and properties

Component	Composition/Specification
Grade	3.7 Ultra High Purity
Methane	99.97% by volume
Oxygen	< 15 ppm
Water (moisture)	< 5ppm
Nitrogen	< 100 ppm
$CO + CO_2$	< 10 ppm
Hydrogen	< 10 ppm
C_nH_m (Other hydrocarbons)	< 100 ppm
Lower Heating Value (60˚F, 14.73 psia)	50 MJ/kg
Molecular Weight	16.3 kg/kmol
Specific Gravity	0.5622

1.3 Low temperature combustion (LTC) concept

Strategies to obviate the use of such expensive and complex engine exhaust after-treatment devices has redoubled efforts to achieve in-cylinder NOx and PM reduction

through low temperature combustion strategies. NOx is observed to form at elevated temperatures upwards of 1900 K (Plee et al. 1981, Flynn et al. 2000, Dec et al. 2000, 1997). Advanced strategies essentially aimed at reducing the in-cylinder temperatures to below this limit have been topic of interest and research pursuits since decades. These strategies, though vast, can be lumped together and named as Low Temperature Combustion (LTC) concepts. Examples of LTC concepts include classical Homogenous Charge Compression Ignition (HCCI), and the more recent Reactivity Controlled Compression Ignition (RCCI), Premixed Charge Compression Ignition (PCCI) and Advanced Low Pilot Injection Natural Gas (ALPING). HCCI is characterized by volumetric autoignition. The Inception of HCCI concepts can be traced back to 1958 (Alperstein et al.) followed by Onishi et al. and Noguchi et al. in 1979. Several other researches have shown tremendous decrease in NOx and soot but an appended taxation in the form of higher HC and CO emissions (Stanglmaier et al. 2001, 1999, Dec et al. 2003. Studies by Krishnan et al. 2002 and Srinivasan et al. 2006 have reported a trade-off between NOx and HC emissions and show decreasing NOx trends with increasing HC with advanced diesel injection timings (300 CAD) in ALPING combustion. Injection strategies (Guerry et al. 2014, Raihan et al. 2014 and Kim et al. 2007) at advanced timing of 310 CAD show very low NOx with high HC and CO emissions, especially at low loads. Their studies indicate that at elevated injection pressures, HC emissions decreased.

1.4 Dual Fuel Combustion

Dual fuel combustion is governed by different engine control levers, viz. pilot fuel injection timing (advanced/retarded injection w.r.t. TDC), pilot fuel quantity, Percentage

Energy Substitution (PES), injection pressure, intake manifold pressure, air intake temperature and employment of hot/cooled EGR. EGR tends to suppress NOx formation by lowering the in-cylinder temperature of the mixture, but it can lead to poor Combustion Efficiency (CE) due to inefficient oxidation of HC and CO (Huestis et al. 2007). Hot EGR can lead to better efficiencies and lower HC up to certain EGR percentages, above which it tends to induce more NOx emissions (Srinivasan et al. 2007 and Qi et al. 2007). Advancing the Start Of Injection (SOI) is an important lever which seems to benefit FCE with either decreased NOx or HC based on other control levers. Advanced SOIs reduced HC and CO emissions, as reported by Abd Alla et al. 2002 with increased FCE, but with an increased NOx. However, their study was limited to an SOI range of 325 CAD to 330 CAD. A similar study with Biodiesel-Diesel combination (Ryu, K. 2013a) showed reduced smoke and NOx. But then again, the study was limited to SOIs at 349 CAD – 337 CAD. Apart from rising HC levels, low NOx, improved FCE at advanced SOIs was also shown by Singh et al. 2004. An SOI sweep on the same SCRE set-up (as in this study) was performed by Dwivedi 2013, achieving very low NOx and smoke while reporting higher HC and CO concentrations. Increase of pilot fuel quantity resulted in improved FCE, lower CO emissions while increased Nitric Oxide (NO) and soot emissions as observed by Papagiannakis et al. 2007. Additionally, improvements in thermal efficiency and combustion noise have been observed (Selim 2004) with an increase in pilot fuel quantity.

Detailed chemical kinetic studies have shown the inevitable trade-off between HC and NOx emissions (Flynn et al. 2000). Thus, an increasing need to address these two emissions simultaneously was felt. Kim et al. 2007 found dual injection of diesel as a

viable alternative to using a combination of premixed injection and direct injection in PCCI diesel combustion. They employed a constant injection pressure of 1000 bar and used narrow spray cone angle injector (60˚). This resulted in CO reduction while no appreciable HC benefits were recorded due to second injection. In another study, Choi et al. 1999 demonstrated reduced soot emissions with little penalty on NOx as a result of split injection while operating on oxygenated fuel blends. Split injection strategies (similar to the one adopted in this study) studied by Carlucci et al. (2014) reveal similar improvements in NOx and CO but with a taxation on HC emissions in dual fuel biodiesel-producer gas combustion.

A conference paper based on some portion of the presented manuscript has been accepted for publication in the 9th U.S. National Meeting of the Combustion Institute (Sohail et al. 2015):

1.5 Research Objectives

This research is focused towards a dual motive of reducing engine-out emissions with coupled increased fuel efficiency benefits. Specifically, is it to :

1. Reduce HC, CO, NOx and soot emissions from a dual-fueled engine.
2. Improve (or at the very least, maintain) the fuel conversion efficiency.
3. Obviate the use of expensive engine exhaust after treatment devices viz. DPF and SCR.

Investigatory experiments were performed on a SCRE dual fueled with pilot injected diesel and port-fueled methane. Two separate injections of diesel fuel were incorporated to quantify their effects on the performance and emissions characteristics of the engine operation.

1.6 Organization of Work

Chapter 1 deals with an introduction to diesel engines. The viability of methane as a surrogate fuel for diesel has been studied and a review of current research from published literature has been presented. Chapter 2 unfolds the details of the engine, experimental instrumentation and strategy used for achieving the stated objective. The engine pressure data along with other recorded pressures, temperatures and flow rates has been used in different formulae to arrive at performance parameters and described in this chapter. A comprehensive explanation of the recorded and calculated performance and emissions parameters has been presented in Chapter 3. Further, the experiments have been summarized and conclusions have been drawn in Chapter 4. Finally, recommendations to undertake future studies along the same strategies have been advocated in Chapter 5.

CHAPTER II

EMISSIONS STANDARDS AROUND THE WORLD

The problems related to emissions are a worldwide phenomenon. This poses a global and rather formidable challenge to the engines researchers. Almost all the countries of the world have their version of the vehicular emissions regulations. But mostly, they can be categorized into three major legislative standards:

1. EPA Standards
2. Euro Standards
3. Japan Standards

There are various other countries which follow their separate emission legislations, chiefly among which are:

- China National Standard
- India or Bharat Stage Standard
- Brazil National Council for the Environment or CONAMA PROCONVE Standards
- Korean Ministry of Environment or KMOE Standard

The most regulated emissions are those of CO, HC, NOx, and PM (soot). In order to have a thorough and comparative understanding of the allowed emissions values of these

effluents, the following table for heavy duty on-road diesel engines is being furnished (Table 2.1). All the reported values are in the units of g/kW-hr.

Table 2.1 Emissions values for different effluents

Current Standard	Since	Reference	Test	CO	HC	NOx	PM
				(g/kW-hr)			
EPA & CARB	2015	-	-	20.79	0.19	0.027	0.013
Euro VI	Jan. 2013	-	WHSC	1.5	0.13	0.4	0.01
Japan	2009	-	JE05	2.22	0.17	0.7	0.01
China V	Feb. 2013	-	ESC + ELR	1.5	0.46	2.0	0.02
India: Bharat Stage IV	2010	Euro IV	ESC	1.5	0.46	3.5	0.02
Brazil: Tier P-7	Jan. 2012	-	ESC/ELR	1.5	0.46	2	0.02
Korea	Jan. 2014	Euro IV	WSHC	1.5	0.13	0.4	0.01

Source: www.dieselnet.com/standards

CHAPTER III

EXPERIMENTAL SETUP AND FORMULAE USED

3.1 Experimental Setup

The layout of the experimental set up is shown in Figure 3.1. The experiments were conducted in a Single Cylinder Research Engine (SCRE) with specifications of the engine in Table 3.1. A 250 HP AC regenerative dynamometer (Dyne Systems), controlled by Interlock V engine controller coupled to the SCRE was used to measure torque and speed.

An integrated emissions bench (Altech Environment S.A.) was used to measure engine-out HC, NOx, CO, CO_2 and O_2 emissions. The emissions bench was calibrated for CO, CO_2 and O_2 using known concentrations of the same gases For calibration of HC, propane was used. Further, for calibration of NOx, a chemical reaction between bottled NO and Ozone (produced after reaction of 100% O_2) provided the NOx gas. The concentrations were: THC 8688 ppm, NOx: 2006 ppm, CO 8 %, CO_2 18 % and O_2 17 %. A sample trolley equipped with heated pump and heated sample lines maintained at 191±5˚C ensured the nucleation, condensation and coagulation of the exhaust particles is avoided. Smoke was measured using an AVL 415S variable sampling smoke meter in Filter Smoke Number (FSN). A TSI Engine Exhaust Particle Sizer (EEPS) spectrometer with a thermo-diluter having dilution factor 1870:1 measured particle sizes and their respective concentrations. Least sized particle size which could be measured was 6

nanometers. A Fourier Transform Infra-Red spectrometer (FTIR) was used to take additional emissions measurements (AVL SESAM i60 FT). The emissions were noted as an average of data recorded over a period of 60 seconds.

Diesel injection in the cylinder was achieved using a Stand Alone Diesel Injector (SADI) controlled by National Instruments' Combustion Analysis Software (NI-CAS) toolkit. A Bosch CP3 common-rail fuel injection pump and injector were employed. Crank-resolved injector needle lift was measured using a Hall Effect sensor (Wolff Controls Corporation, Winter Haven, Florida). Ultra Low Sulfur Diesel (Sulfur 15 ppm, cetane number CN40 minimum, Rackley Oil, Starkville MS) fuel and methane (Ultra high purity 99.97 %, NexAir, Memphis TN) were used for fuelling the engine. The diesel was red-dyed (with solvent Red 164, 11.1 ppm) and tax exempt. Detailed specification of the diesel used in this study is furnished in Table 3.2. Methane fumigation in the air intake manifold was controlled using a current controlled electronic needle valve (Model MCM-050AB, Hanbay corp., Montreal, Canada). Diesel and methane flow were monitored using Emerson Micro Motion Coriolis flowmeters. The diesel temperature was regulated by a fuel heat exchanger (Model SSCF, Standard Xchange, Buffalo, NY). In-cylinder pressure was monitored using a Kistler 6052C pressure transducer and a Kistler 5010B charge amplifier. The pressure transducer was bored on the cylinder head and its flush seating with the inner periphery of the cylinder head was assured to mitigate any pipe oscillations. An AVL Indismart data acquisition system collected the cylinder pressure and needle lift data over 1000 cycles. Other transient data, including Maximum Pressure Rise Rate (MPRR), Coefficient of Variation (COV), Ignition Delay, Combustion Phasing (CA50) and Net Indicated Mean Effective

Pressure (IMEP) were also ensemble-averaged over 1000 cycles. A BEI incremental shaft encoder (Model no. XH25D-SS-3600-ABZC-28V/V-SM18) with a resolution of 0.1 crank angle degrees (CAD) was connected to the engine crankshaft to trigger cylinder pressure data acquisition. The encoder TDC and the physical engine TDC were software phased to ensure crossover-free motoring pressure traces. In-cylinder pressure was pegged to the intake manifold pressure at BDC using an intake manifold absolute pressure sensor (Model: Setra 209, accuracy 0.25%).

Type-K thermocouples were used for temperature measurements (Omega Engineering INC., Stamford CT). Engine Oil Temperature Conditioner (EOTC) and Engine Water Temperature Conditioner (EWTC) with PID (Automation Direct) control loops maintained the engine oil and coolant water temperatures respectively at 80 °C. The cooling needs were provided by an external 10000 gallon water tank and pump system. An air compressor (Model GA75, Atlas Copco Airpower, Belgium) coupled with heatless desiccant dryer (Model CD250, Atlas Copco Airpower, Kenosha, WI) was used to simulate intake air boost. A sonic orifice flowmeter (Flow Maxx Model SN16-SA-235) measured the intake air mass by ensuring choked flow across its orifice and recording the upstream pressure and temperature. The various accuracies of measurements have been listed in Table 3.3.

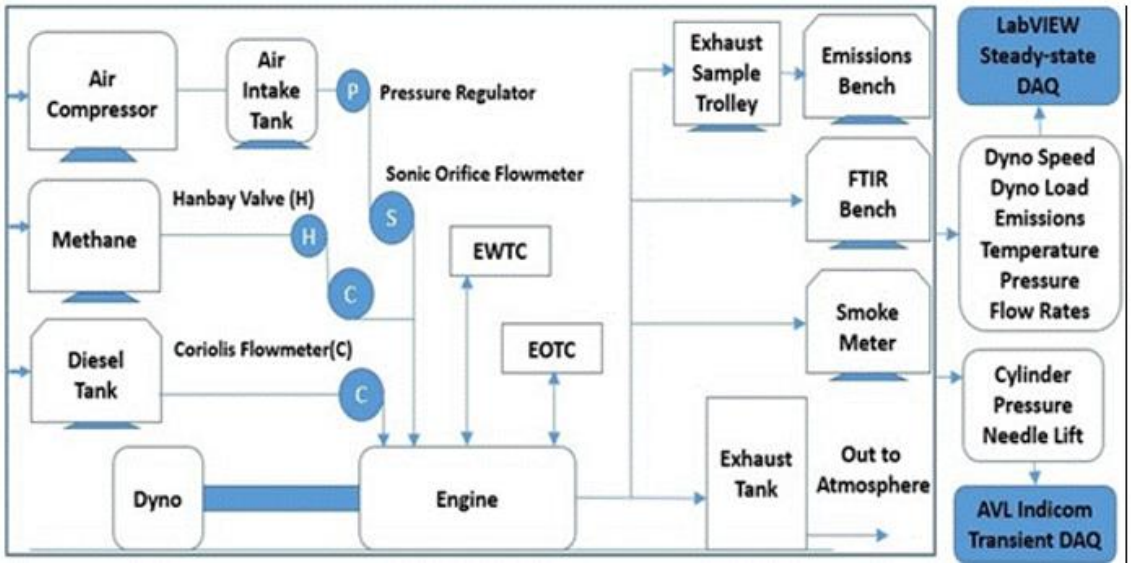

Figure 3.1 Schematic of experimental equipment layout

Table 3.1 Engine Specifications

Parameter	**Specification**
Engine Type	Rsi-130 Doosan DV-11 SCRE
No. of cylinders	1
Displacement Volume	1.827 Liters
Compression Ratio	17.1:1
Maximum Engine Speed	1900 RPM
Combustion chamber	Mexican hat
Valve Train	2 Intake, 2 Exhaust valves
Valve Timings	IVO : 32 CAD, IVC : 198 CAD EVO : 532 CAD, EVC : 14 CAD
Bore x Stroke	128 x 142 (mm x mm)
Connecting rod length	228 mm
Diesel Pump	Bosch CP3 Pump
Injection System	Electronically controlled Common-rail
Injector nozzle hole diameter	0.197 mm
Number of nozzle holes	8

Table 3.2 Composition and Specification of diesel

Property	Unit	Specification
Vendor	-	CITGO CORP.
Specific Gravity, min.	Unit less	0.876
Cetane Number, min.	Unit less	40
Aromatics, max.	% volume	35
Flash Point	˚C	52
Viscosity	m^2/s	(1.9 to 4.1) x 10^{-6}
Pour Point	˚C	-18 to -12
Cloud Point	˚C	-9 to -7
Sulfur, max.	ppm	15
Ash	% weight	0.01
Water & Sediment	% volume	0.05

Table 3.3 Accuracies of Experimental Measurements

Measured parameter	Manufacturer	Model	Unit	Conc.	Accuracy
Engine speed	Dyne Systems	Interlock V	RPM	-	± 1 rpm of reading
Engine torque	Dyne Systems	Interlock V	Nm	-	± 0.06% of reading
Cylinder pressure	Kistler	6052C	bar	-	±0.005 of reading
Diesel flow rate	Micro Motion		kg/h	-	±0.05% of reading
Methane flow rate	Micro Motion		kg/h	-	±0.35% of reading
Air flow rate	Flow Maxx	SN16-SA-235	kg/h	-	±0.1% of reading
Temperatures	Omega	Type-K	°C	-	±0.75% of reading
Pressures (intake, exhaust, coolant & lubrication oil)	Omega, Setra		psig	-	±0.25% of reading
Smoke number	AVL	415S	FSN	-	±0.001 of reading
THC emissions	ESA	FID	ppm	8688	<0.5% of full scale
NOx emissions	ESA	CLD	ppm	2006	<1% of full scale
CO	ESA	NDIR	%	8	<1% of full scale
CO2	ESA	NDIR	%	18	<1% of full scale
O2	ESA	Paramagnetic Analyzer	%	17	<1% of full scale

3.2 Experimental Strategy and Matrix

The experiments were conducted at steady-state i.e. the engine was allowed to output constant BMEP, PES and intake manifold pressure for 30 seconds before the start of data recording. The data points were selected in a calculated manner that result in a gradual decrease of HC, NOx, CO and Smoke emissions. The experiments were repeated three times and standard error bars (68% confidence interval) indicate measurement variability (not uncertainty). Each set of these experiments covers 22 data points, denoted by Operating Point Number (OP#). For ease of understanding, all the OPs have been tabulated in a matrix in Table 3.4. The first operating point was chosen to be for single injection at 310 CAD, which serves as the baseline for performance and emissions comparison. The first engine operating conditions were 1500 rev/min, producing 5 bar BMEP, injecting fuel at 500 bar P_rail and 310 CAD using 1.5 bar of intake air boost. No EGR was employed for the tests. Raihan et al. (2014) reported the optimum PES running at these conditions as 85 PES, which has been adopted as the initial PES for the experiments in this study. The baseline performance and emissions values are found to be: HC-29.6 g/kW-hr, NOx-0.43 g/kW-hr, CO-5 g/kW-hr, smoke-0.03 FSN, IFCE-44.2% and COV-1.7%. Secondary fuel injection was employed for all the data points starting at OP #2. For OP #2, first a closed coupled injection (second injection being at 320CAD) was tried to see its effects on emissions, HC decreased considerably with steep increase in NOx. The secondary injection timing for OP #3 is chosen to be further retarded and taken at 325 CAD. As a result, a decrease in NOx but a coupled increase in HC emissions is observed.

The closed coupled dual injections didn't seem to be paying off well in terms of emissions. There was an increase in ISCO and ISNOx with a slight decrease in fuel efficiency. Consequently, OP #4 was tried at a second injection timing of 370 CAD which is after TDC. Also, the PES was dropped to 75 PES, as high MPRRs and corresponding unstable engine operation were encountered at 85-80 PES. A phenomenal decrease in NOx is reported (from 6.7 g/kW-hr to 0.6 g/kW-hr) with an increase in the HC (from 23.8 g/kW-hr to 31.4 g/kW-hr) when OP#3 is compared to OP#4. While all the parameters are kept same other than the injection pressure and second injection timing change to 375 CAD, the next data point at OP#5 exhibited even lower HC and NOx emission values. This OP can be attributed as the first data point after which simultaneous decrease of HC and NOx can be realized. Further, OP #6 onwards the reduction in CO is also observed.

Keeping first injection timing at 310 CAD and the second at 375 CAD for all subsequent data points, the benefits of varying the P_rail was studied. This P_rail study is referenced by the literature (Jindal et al. 2010 and Carlucci et al. 2008) that with the increase in the fuel injection pressure, the diesel fuel molecules get dispersed in the combustion chamber even more, leading to its increased mixing & better combustion with lower unburnt HC emissions. The experiments were performed till a maximum of 1500 bar P_rail. Multiple data points are presented for 1000 bar P_rail to demonstrate the coupled inverse relationship of HC and NOx emissions at the same injection pressure. As can be observed from the comparison of OP #9, 10 and 11, there is a definite trade-off between the two emissions values. While NOx decreases from 1.43 g/kW-hr to 0.67 g/kW-hr, the HC increases from 12.3 g/kW-hr to 16 g/kW-hr. It is important here to note

that such a major change in the emissions at the same injection pressures is due to the duration of the two injections (1st 0.52 ms and 2nd 0.21 ms to 1st 0.49 ms and 2nd 0.315 ms).

Such inverse relationship trends are also observed at multiple data points at same P_rails of 800, 900 and 1000 bar. Owing to this trade-off, a single best point with the best performance and emission results can't be nominated. But, the OP #19 can be regarded as the optimal data point where the values are: HC-13.08 g/kW-hr, NOx-0.5 g/kW-hr, CO-2.84g/kW-hr, smoke-0.06 FSN, IFCE-48.7% and COV-1%. This is an overall improvement in the emissions and performance characteristics with the corresponding percentage improvement of: HC-56%, NOx-(-16%), CO-43%, smoke-50%, IFCE-10% and COV-41%.

Table 3.4 Experimental Test Matrix

OP (#)	RPM (rev/min)	P_in (bar)	Engine Load (BMEP, bar)	PES (%)	Rail Pr. (bar)	1st Inj. (CAD)	Dur. (ms)	2nd Inj. (CAD)	Dur. (ms)
1	1500	1.5	5	85	500	310	0.52	NA	NA
2	1500	1.5	5	85	500	310	0.425	320	0.425
3	1500	1.5	5	85	500	310	0.436	325	0.436
4	1500	1.5	5	75	500	310	0.52	370	0.42
5	1500	1.5	5	75	500	310	0.52	375	0.49
6	1500	1.5	5	75	550	310	0.52	375	0.465
7	1500	1.5	5	75	600	310	0.52	375	0.35
8	1500	1.5	5	75	650	310	0.52	375	0.31
9	1500	1.5	5	75	700	310	0.52	375	0.192
10	1500	1.5	5	75	700	310	0.5	375	0.29
11	1500	1.5	5	75	700	310	0.49	375	0.31
12	1500	1.5	5	75	800	310	0.45	375	0.29
13	1500	1.5	5	75	800	310	0.46	375	0.265
14	1500	1.5	5	75	900	310	0.42	375	0.28
15	1500	1.5	5	75	900	310	0.46	375	0.17
16	1500	1.5	5	75	1000	310	0.45	375	0.135
17	1500	1.5	5	75	1000	310	0.405	375	257
18	1500	1.5	5	75	1100	310	0.39	375	0.25
19	1500	1.5	5	75	1200	310	0.385	375	0.255
20	1500	1.5	5	75	1300	310	0.36	375	0.275
21	1500	1.5	5	75	1400	310	0.325	375	0.295
22	1500	1.5	5	75	1500	310	0.325	375	0.32

3.3 Definitions

For the sake of clarity, parameters such as equivalence ratio (Φ_{flow}), percent energy substitution (PES), ignition delay (ID), combustion efficiency (η_c), indicated fuel conversion efficiency (IFCE), apparent heat release rate (AHRR), and the ratio of specific heats (γ) are defined below:

$$PES = \frac{\dot{m}_g LHV_g}{\dot{m}_d LHV_d + \dot{m}_g LHV_g} * 100\% \quad (3.1)$$

$$\Phi_{flow} = \frac{\left(\frac{A}{F}\right)st-tot}{\left[\frac{\dot{m}_a}{\dot{m}_g + \dot{m}_d}\right]} \quad (3.2)$$

$$ID = CA5 - SOI \quad (3.3)$$

$$\eta_c = 1 - \frac{\sum_i x_i Q_{LHV_i}}{[\dot{m}_f/(\dot{m}_a + \dot{m}_f)\,]\,\dot{Q}_{LHV_f}} \quad (3.4)$$

$$\text{IFCE} = \frac{IP}{\dot{m}_d LHV_d + \dot{m}_g LHV_g} \quad (3.5)$$

$$AHRR\,(\theta) = \frac{\gamma}{\gamma-1} P \frac{dV}{d\theta} + \frac{1}{\gamma-1} V \frac{dP}{d\theta} \quad (3.6)$$

$$\gamma(T) = 1.338 - 6 \times 10^{-5} T + 1 \times 10^{-8} T^2 \quad (3.7)$$

In Equations 3.1 and 3.2, ṁ refers to the mass flow rates of diesel (subscript d), methane (subscript g), and air (subscript a), and *LHV* refers to the lower heating values of the corresponding fuels. Stoichiometric air-fuel ratio $(A/F)_{st\text{-}tot}$ is defined as the stoichiometric air required for complete oxidation of both diesel and methane into CO_2 and H_2O. Therefore, $(A/F)_{st\text{-}tot}$ depends on methane PES. The start of combustion is defined as CA5, or the crank angle at which 5 percent of cumulative heat release occurs. Also, CA10-90, which is defined as the difference between the crank angle at which 10 percent of cumulative heat release occurs and the crank angle at which 90 percent of cumulative heat release occurs, gives an estimation of overall combustion duration. Combustion phasing is defined as the crank angle at which 50 percent of the cumulative

heat release occurs and denoted as CA50. Ignition delay is the difference between CA5 and SOI.

In Equation 3.4, combustion efficiency (η_c) is normally calculated using the mass fractions (x_f) of CO, H_2, HC and PM and their respective LHVs. Since the composition of HC in the exhaust, and thus its LHV, are not known, Heywood recommends using the LHV of the fuel as they are expected to of comparable magnitude (Heywood 1988). However, for this study, since two fuels were used, the combined mass-fraction-weighted LHV of diesel and methane is used to represent the LHV of HC. The lower heating values for methane, CO and H_2 are assumed to be 50.0 MJ/kg, 10.1 MJ/kg and 120 MJ/kg, respectively. Also, since gravimetric PM was not measured in the present experiments, it was not considered in the combustion efficiency calculations. The net IFCE was calculated following Equation 3.5 using the net indicated power estimated from the measured in-cylinder pressure data and the measured fuel flow rates and their respective LHVs. Equation 3.6 dictates the net apparent heat release rate (AHRR) which was derived from the measured in-cylinder pressure data. The instantaneous volume (V) was calculated from the engine geometry and derivatives of pressure and volume ($dP/d\theta$ and $dV/d\theta$) were calculated numerically using a four point central difference formula. The specific heat ratio (γ) shown in Equation 3.6 was evaluated as a function of mass averaged temperature (T) using Equation 3.7 (Brunt et al. 1998).

The in-cylinder combustion pressure typically varies as a function of the crank position. Brake Mean Effective Pressure (BMEP) the hypothetical constant pressure which acts on the piston throughout the cycle, such that the amount of brake work produced is equal to the actual brake work produced from a real combustion cycle (with

variable pressure). BMEP is a theoretical manifestation of the in-cylinder pressure which allows comparison among engines of different volumetric displacements. Owing to this convenience, BMEP has been used in this study for characterization of the OPs. It is a derived quantity which is a function of the engine torque (τ) measured by the dynamometer, volumetric displacement (V_d) of the engine and the number of engine strokes (n_R):

$$BMEP = \frac{P_b . n_R}{V_d . N} = \frac{4\pi\tau}{V_d} \tag{3.8}$$

Equivalence ratio has been calculated in equation 3.2 based on the mass flow rates of air and fuel. Additionally, the Equivalence ratio can also be calculated based on the engine-out emissions, as:

$$\Phi_{emissions} = \frac{2\, n_{O2}}{n_p X_{H2O} + n_p (1 - X_{H2O})(\mathrm{X}_{CO} + 2\mathrm{X}_{CO2} + 2\mathrm{X}_{O2} + X_{NO} + 2X_{NO2})} \tag{3.9}$$

Where X_i and X_i are the wet and dry mole fractions of species "i", respectively.

Since the two equivalence ratios are calculated using two separate sets of equipment, a close match (usually within ±5%) between the two values verifies that the overall performance and emissions results are accurate.

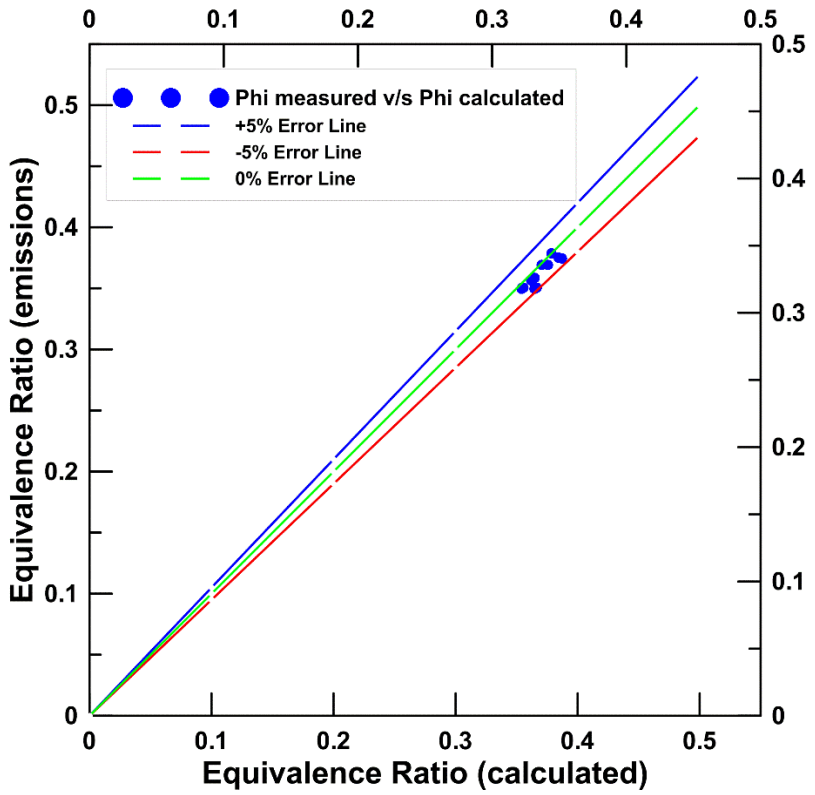

Figure 3.2 Equivalence ratio (emissions) versus equivalence ratio (calculated) for diesel-methane experiments in this study

The HC, CO and NOx emissions are usually measure in parts per million (ppm) or as a percentage of the total exhaust gas flow. Much like the BMEP, to enable comparison of emissions species among different engines, these percentage values have to be converted into Brake Specific Emissions (BSE) in the units of g/kW-hr. This is also the unit which is used in the world emissions standards in Table 2.1. The BSE calculations are as follows:

$$BSE = \frac{\dot{m}_{fuel}}{P_b} \times X_{species} \times [1 + \frac{\left(\frac{A}{F}\right)_{st}}{\Phi_{emissions}}] \quad (3.10)$$

Where $X_{species}$ is the mass fraction of the particular emission species.

CHAPTER IV

PERFORMANCE AND EMISSIONS

For all of the performance and emissions characteristics, Operating Point #1 has been considered as the baseline for reference, since the study of effects of the dual injection deployment is the objective of this investigation.

4.1 Cylinder Pressure and Net Apparent Heat Release Rate, Needle Lift and Global Temperature

Figs 4.1 (a) and 4.1 (b) show the cylinder pressure schedules for the 22 operating points enlisted in Table 3.4. For the ease of readability, these data points are broken up in two graphs covering 11 operating points each. For the single injection regime at OP #1, the cylinder pressure peaks after TDC. For subsequent increase in injection pressure, there is a corresponding increase in the peak pressure accompanied with the profile phasing even closer to the TDC. For example, when OP #5 and 6 are compared, an increase in peak pressure (from 102 bar to 108 bar) and corresponding closer phasing w.r.t. TDC (from 366 CAD to 365 CAD) is observed. This phenomenon may be attributed to increased momentum of the jet with increasing injection pressures leading to better local mixing and dispersion of diesel fuel, thereby, increasing the number of ignition centers and faster combustion rates reflected by more advanced CA50. It is well known from literature that combustion phasing just after TDC yields the best possible fuel conversion efficiency.

Further, for the OPs of same injection pressure, there is a fall of pressure accompanied with closer phasing w.r.t. TDC, if the first injection duration is lesser. For instance, when OP #9 and 10 are compared, there is a reduction in peak pressure (from 126 bar to 122 bar) coupled with its phasing after TDC (from 361 CAD to 362 CAD). This is due to the decrease in the diesel flow rate associated with the decreased injection duration. The corresponding CA50 is also found to be closer to TDC.

The AHRR profiles are depicted in Figs. 4.2 (a) and (b). The AHRR trends follow the cylinder pressure trends in that the increase in fuel injection pressure demonstrates a corresponding increase in AHRR magnitude along with an advanced phasing of AHRR profile and vice versa. OP #2 and OP #3 show comparatively inconsistent trends due to the second injection being added very close to the first injection (at 320 CAD and 325 CAD for OP#2 & OP #3, respectively). This decreases ignition delay as seen in Figure 4.5 and results in earlier combustion phasing. The later OPs have been conducted with a second injection well after the TDC (at 375 CAD), which allowed the second injection to provide additional combustion energy to burn-off HC emissions. The figures show the presence of three distinct areas on the profile of each operating point (except OPs #1, #2 and #3 as the second injection isn't there for OP #1 and the second injection is done just next to first injection for OPs #2 and #3. These OPs, however, show 2 stage heat release). Along with the main heat release event, there is a Low Temperature Heat Release (LTHR) occurring at about 340 CAD and a third heat release event at the second injection timing. It is evident from the literature that LTHR is more likely to occur below global temperatures of 850 K (Saxena and Bedoya, 2013),

very likely from the first diesel injection, followed by the ignition of the methane-air mixture, and the extended heat release from the late second injection

Trends similar to cylinder pressure profiles are observed for AHRR. The reduction of AHRR and its more retarded phasing also hold true for the same injection pressure operating points when the injection duration is reduced. For the same injection pressure operating points when the injection duration is reduced, a reduction of AHRR and its retarded phasing are also observed. This is also in confirmation with the cylinder pressure profile. This trend may be attributed to better diesel dispersion with increase in fuel injection pressure.

The magnitude of LHTR successively decreases for higher injection pressures. This can be related to the greater fuel-air mixing achieved at higher injection pressures. Decreasing LTHR may also be due to fuel impingement on the walls and not available for ignition with increased injection pressure.

The corresponding needle lift curves in Fig. 4.1 (a) and (b) show the start of injection (SOI) and the injection duration for each OP. The unit of needle lift is arbitrary as the SOI and injection duration data is enough to gain referential perspective. Further, ripples on the needle lift curve after the first lift are due to the noise of the needle lift sensor.

Figures 4.3 (a) and (b) show the global temperature schedules for these OPs. The LTHR peak is found to be lower for OP #7 and OP #9 as compared to OP #6 and OP #8 owing to their comparatively lower first injection duration. Also, their phasing is found to be more retarded. Bulk temperatures affect HC and CO emissions. The oxidation of fuel into intermediate HC and CO and in turn, their oxidation to CO_2 increases the in-

cylinder bulk temperature. A reduction in both HC and CO is observed as the global temperatures are seen to increase, especially after OP #7, maintaining about 1400 K. The last two OPs again show heightened HC and CO emissions as the peak global temperature also decreases.

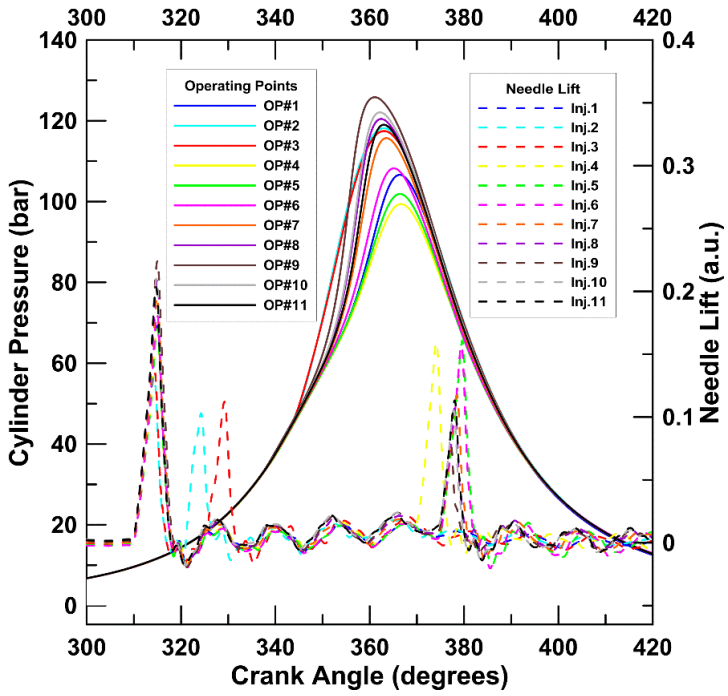

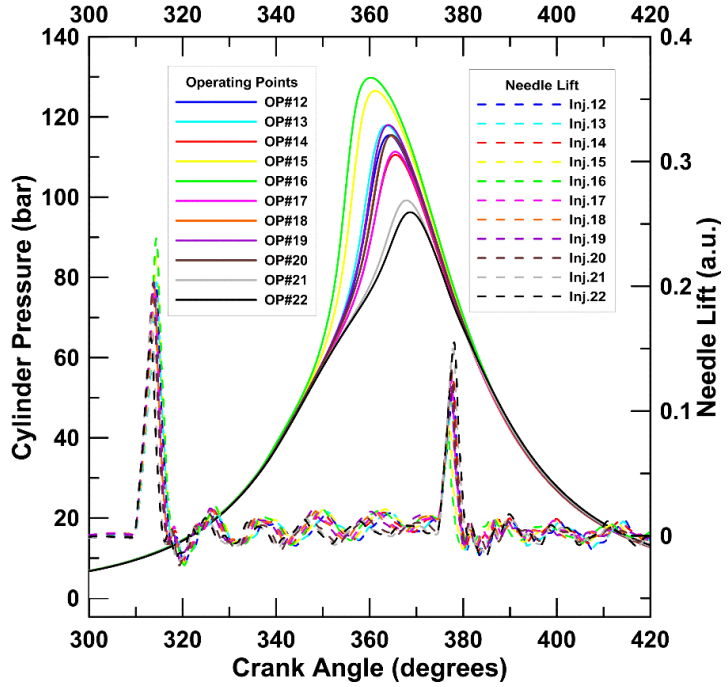

Figure 4.1 Cylinder Pressure schedules

(a): OP #1-11 at N=1500 RPM, P_in=1.5 bar, and BMEP=5
(b): OP #12-22 at N=1500 RPM, P_in=1.5 bar, and BMEP=5

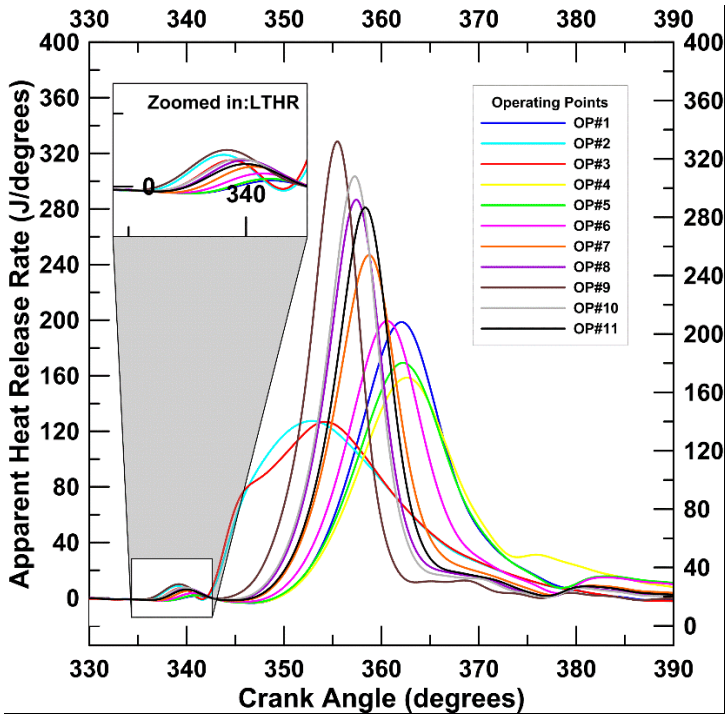

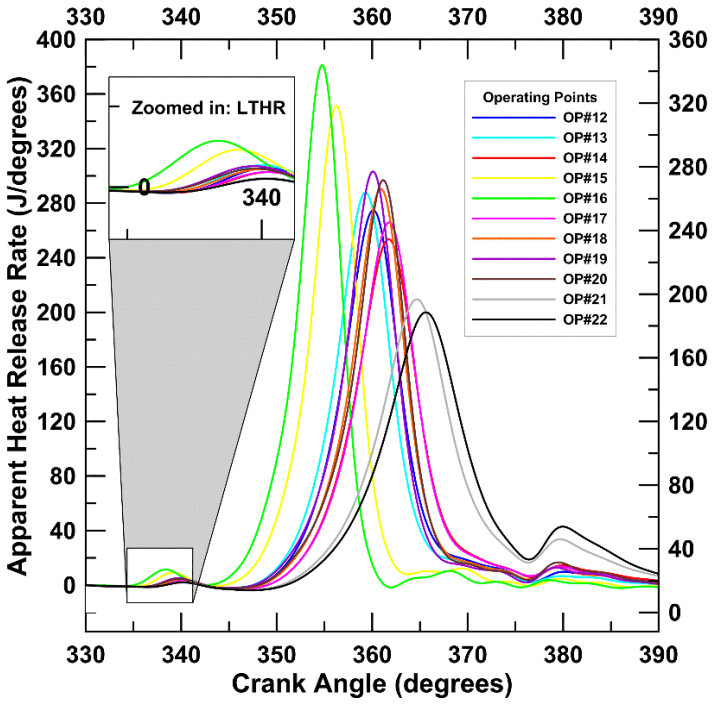

Figure 4.2 AHRR schedules

(a): OP #1-11 at N=1500 RPM, P_in=1.5 bar, and BMEP=5
(b): OP #12-22 at N=1500 RPM, P_in=1.5 bar, and BMEP=5

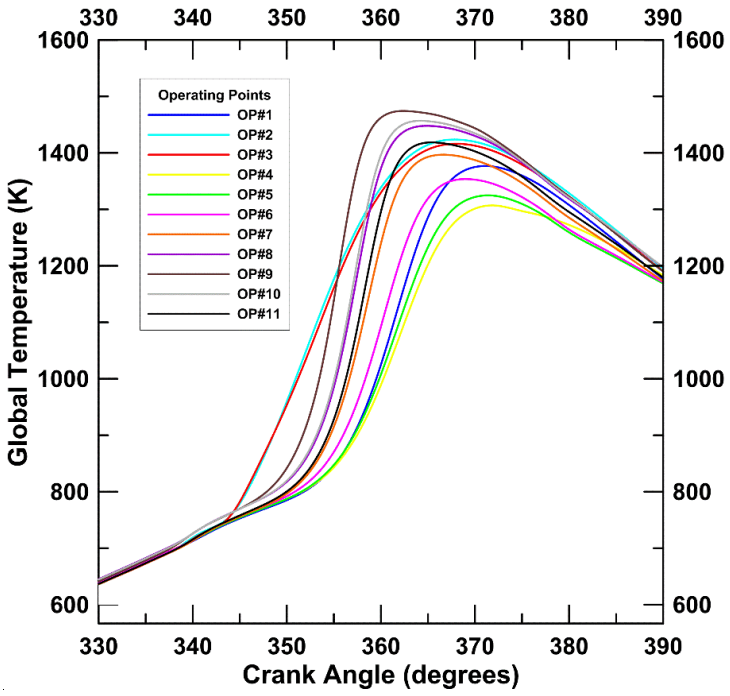

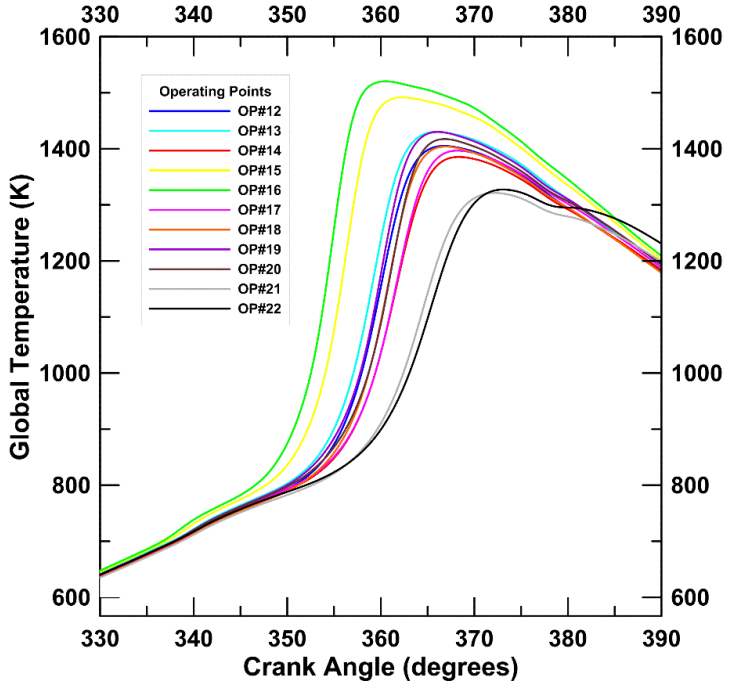

Figure 4.3 Global Temperatures

(a): OP#1-11 at N=1500 RPM, P_in=1.5 bar, and BMEP=5
(b): OP#12-22 at N=1500 RPM, P_in=1.5 bar, and BMEP=5

4.2 Indicated Fuel Conversion Efficiency (IFCE) and Combustion Efficiency(CE)

The combustion efficiency profiles in Figure 4.4 show a generally increasing trend. This is owing to the observations that both HC and CO are being combusted increasingly well as the injection pressures are raised. This "more complete" combustion leads to better overall burning of the chemical fuel mixture. The highest combustion efficiency is registered at OP #16, where the CA50 and CA10-90 occur at their lowest 354 CAD and 7.5 degrees respectively. This may be attributed to an earlier combustion event which results in almost complete conversion of chemical fuel into its products. A relatively low ID of 38˚ also bears testimony to the fact that the earlier SOI resulted in better Combustion Efficiency (CE).

No appreciable increase in IFCE trends is noticed for the first 5 operating points. The AHRR profiles for these points show the corresponding peaks to be below 200 J/CAD. The peak AHRR increases with each subsequent point when the injection pressures are increased. The best IFCEs are 49.3% and 48.7% which occur for OP # 14 and OP #19 for which the AHRRs are found to be 250 J/CAD and 303 J/CAD respectively. The CA50 profiles show that the phasing of these points are very close to TDC at 361 CAD and 360 CAD respectively. Also, fairly high ignition delay of about 44 CAD which corresponds to about 5 ms also provides ample time for well mixed condition of the fuel-air mixture.

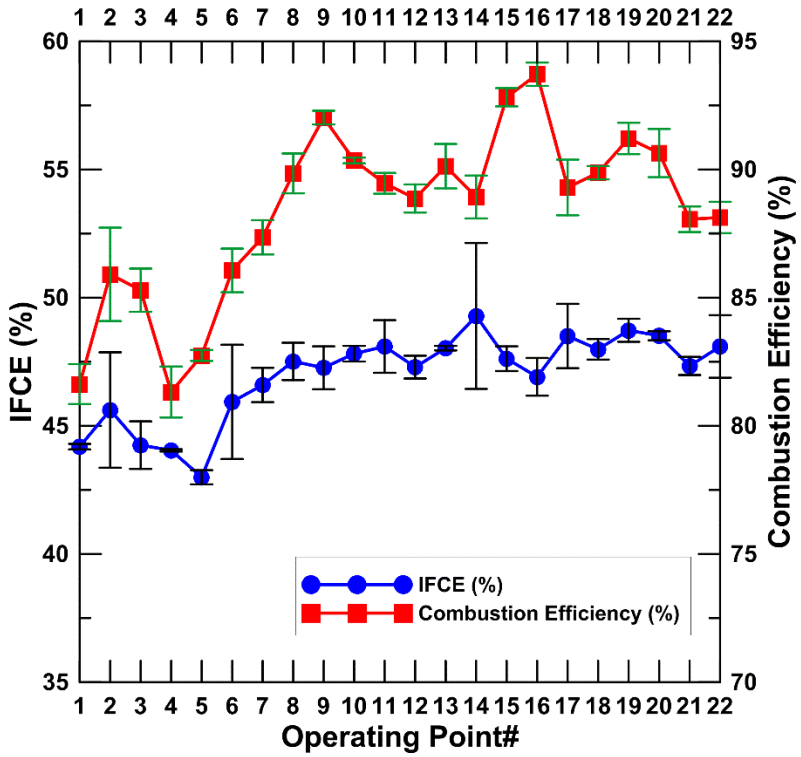

Figure 4.4 IFCE & Combustion efficiency schedules

N=1500 RPM, P_in=1.5 bar, and BMEP=5

4.3 MPRR, Ignition Delay, COV & Combustion Phasing

4.3.1 MPRR, Ignition Delay and COV

The MPRR is observed to increase from OP #1 to OP #2, then decrease till OP #4 (Figure 4.5). Further, it increases steadily till OP #9 due to increased injection pressure, after which it is observed to decrease till OP # 14. Beyond this, the MPRR increases with increasing injection pressure till OP #19. OP #20 onwards a decreasing trend in MPRR is observed with an increase in COV, hinting that the engine has a tendency to misfire and so, lower AHRR and pressure rise rates are noticed. At points of same injection pressure, ones with lower first injection duration have lower MPRR.

Ignition delay is the difference between the end of injection and start of combustion (marked by CA5). ID is observed to decrease for OPs 2 and 3 due to the second close-coupled injection, which provides ample fuel-rich regions favoring an early SOC. However, the ID increases for OPs 4 and 5 as the secondary injection is retarded to 370 CAD and 375 CAD respectively, thereby providing the air-fuel mixture from first injection with enough time to make a homogenous charge. Also, ID is seen to increase for OPs 14, 17, 18, 21 and 22 owing to the increased injection pressure, which disperses the diesel fuel even more, making the mixture leaner. The increase in ID for same injection pressure points is likely due to lower first injection duration between operating points 9-11, 13-12, 15-14 and 16-17. Conversely, the decreased ID for OPs 15 and 16 are likely due to the higher first injection duration (Experimental test matrix, Table 2.3).

The COV remains fairly constant from OP #1 to OP #20. The COV increases abruptly for 85 PES with second injection at 370 CAD, but it is not reported in the present results. Unstable operating conditions were encountered for OP #21 and OP #22 at 1400 bar and 1500 bar injection pressures respectively as the engine had a tendency to misfire.

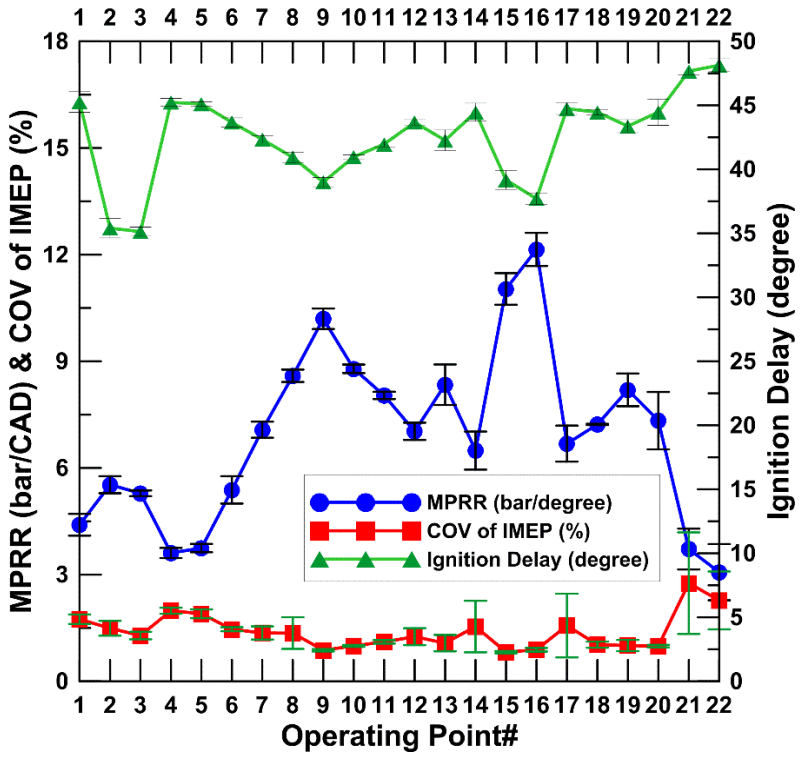

Figure 4.5 MPRR, COV of IMEP & Ignition Delay schedules

N=1500 RPM, P_in=1.5 bar, and BMEP=5

4.3.2 CA5, CA50 and CA10-90

The CA5, CA50 and CA10-90 profiles have been illustrated in Figure 4.6. All the three replicate each other to some degree regarding the rise and fall in profile when shifting to subsequent operating points. The only anomaly is from OP #1 to OP #2 which observes an earlier CA5 and CA50 but an increased CA10-90. This may be attributed to the deployment of the second injection starting from OP #2. With higher injection pressure, the combustion is observed to phase closer to the TDC. Also, a retarded phasing of each CA5 and CA50 with an increased CA10-90 is reported for the lower first injection duration OPs at same injection pressures. This is likely due to smaller amount of diesel fuel and consequently reduced ignition centers. This leads to increased

residence time of the fuel molecules and aids in retarded combustion. This is well corroborated by the ID at these points which increases with increasing CA5, CA50 and CA 10-90.

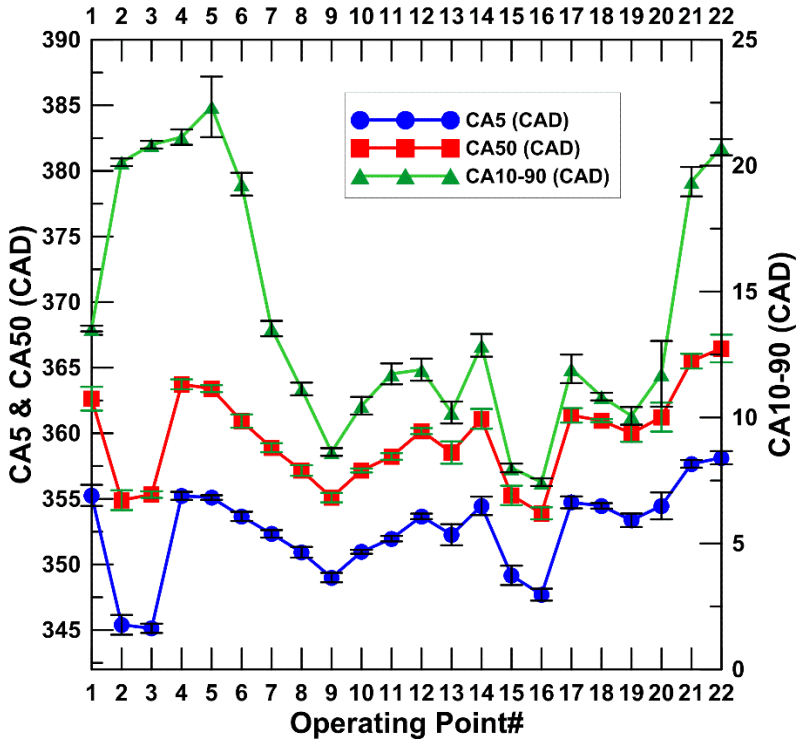

Figure 4.6 CA5, CA50 and CA10-90 schedules

N=1500 RPM, P_in=1.5 bar, and BMEP=5

4.4 Emissions

4.4.1 ISNOx and Smoke trends

The ISNOx schedules are demonstrated in Figure 4.7. ISNOx values increase significantly from 0.43 g/kW-hr to 6.97 g/kW-hr for OP #2 and 3 when compared to OP #1. This is because of the second injection timed very close to the first injection. Closely coupled injection provides fuel in ample quantity to abruptly raise the temperatures of local zones. Thereby the bulk temperature is increased as evident from Figs. 4.3 (a) and

(b). The next injections are done quite farther away from the first and into the expansion stroke. Consequently, the number and peak of local temperature zones are decreased. Thus, the formation of NOx decreases to 0.6 g/kW-hr for OP #4. OP # 5 to OP #9 show marginally increasing trend of NOx due to the raised injection pressure from 550 bar to 700 bar P_rail. At the same P_rail of 700 bar for OP #9 to OP#11, a decreasing trend of NOx is observed as the first injection duration is lowered from 0.52 ms to 0.49 ms. This is attributed to the increased amount of diesel fuel injected, leading to greater local and consequently global temperatures. In addition, the ignition delay is also increased for these low NOx points, providing diesel with more time to mix. Such NOx dependence on first injection duration is also observable for operating points at 800 bar, 900 bar and 1000 bar. Further increase of injection pressure yields NOx values around 0.5-0.6 g/kW-hr.

The smoke emissions illustrated in Fig. 4.7 show an increasing trend till OP#5. OP# 1 to OP#5 are at same injection pressure of 500 bar, but the injection fuel quantity is increased subsequently. As a result, a proportionate increase in soot is observed. As the injection pressure is further increased, the smoke values decrease and remain low till the last OP. This is due to increased momentum of diesel jet, which enables greater entrainment & mixing, thereby resulting in reduced smoke emissions.

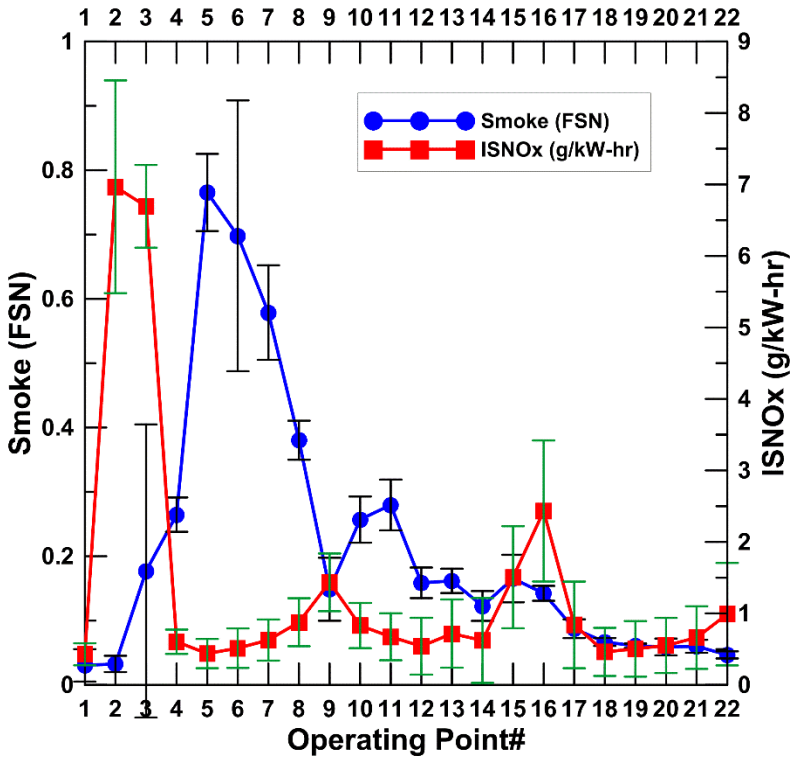

Figure 4.7 Smoke and ISNOx schedules

N=1500 RPM, P_in=1.5 bar, and BMEP=5

4.4.1.1 FTIR emissions values:

An independent measurement of NOx by FTIR (Figure 4.8) spectroscope reveals that the emission levels recorded by the two devices (E.S.A. emissions bench and FTIR) are in close agreement. The units here are parts per million (ppm).

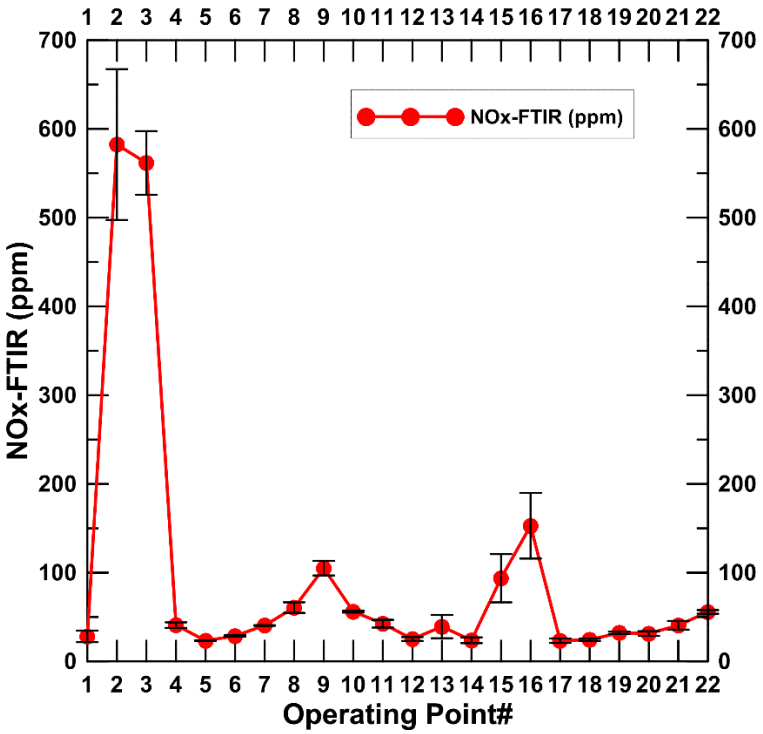

Figure 4.8 NOx schedules-FTIR

N=1500 RPM, P_in=1.5 bar, and BMEP=5

4.4.2 ISHC and ISCO trends

The ISHC schedules are demonstrated in Figure 4.9. A sudden drop in ISHC emissions is seen for OP #2 and OP #3. When temperature profiles for these two points are studied, they show an increase in peak temperature. Also, the CA50 trends show that 50% of combustion energy has been released by 355 CAD, i.e even before reaching TDC. Moreover, the close coupled second injection for these two points result in more combustion energy release to burn off the HCs at an earlier stage. Thus, the rapid combustion results in such a drop in the observed ISHC values. Further, an increase in ISHC at OP #4 is observed. This point onwards, subsequently decreasing trends of ISHC is witnessed because of the increase in diesel injection pressure. Higher P_rail leads to

better fuel-air mixing, more homogeneous combustion and reduction in ISHC emissions. Moreover, the decrease in ISHC emissions is due to the 2nd injection which burns off the unburnt HCs from 1st injection. While for the same injection pressure, OP #9 to OP#11 indicate the dependence of ISHC on duration of first injection. Greater the duration of first injection, greater were the HC emissions. Similar results are seen between operating points 13-12, 15-14 and 16-17.

The ISCO trends shown in Figure 4.9 very closely resemble those of ISHC. The ISCO is observed to decrease from 5.09 g/kW-hr to 4.73 g/kW-hr from OP #1 to OP#2. Then it steadily increases up to about 32 g/kW-hr for OP # 4 and 5, after which it decreases and assumes a value of 3.22 g/kW-hr for OP #20. The last two data points at OP #21 and OP #22 show a sudden increase in ISCO emissions. These trends can be explained in the same manner as of ISHC. Higher emissions till OP #5 is due to the steady increase in first injection duration, greater and earlier fuel entrainment and corresponding higher peak bulk temperature. The decreasing ISCO for OP #6 and beyond is due to the increased injection pressure leading to greater fuel entrainment, shorter flame travel length, smaller CA10-90, more homogeneous mixture and higher combustion rate. The increase in ISCO emissions for the same injection pressure points is also due to higher amount of fuel entering the combustion chamber. The last two operating points show a sharp increase in ISCO emissions as the COV increases from 1% to 2.7%, leading to relatively unstable engine operation.

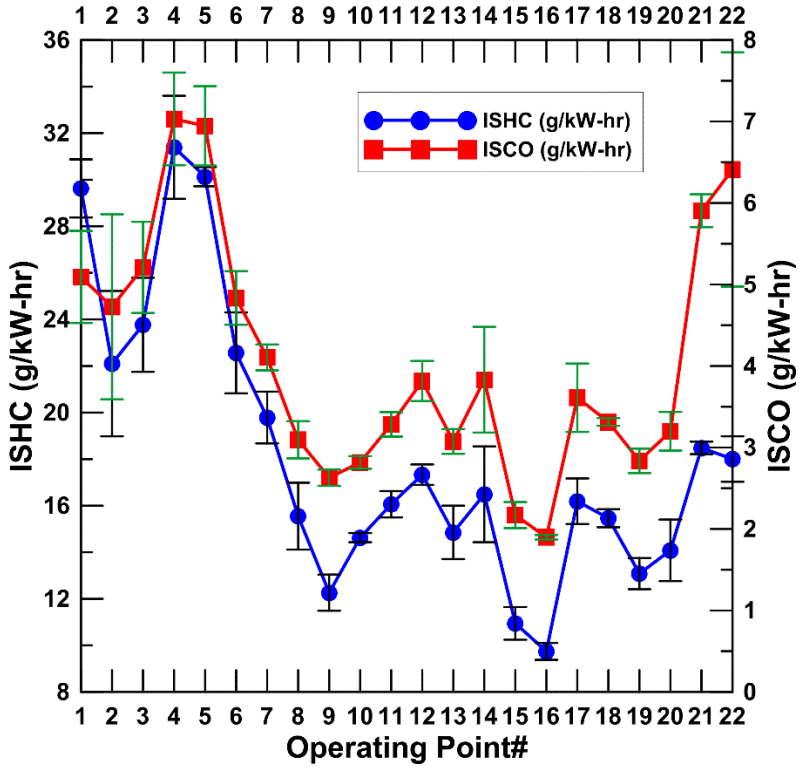

Figure 4.9 ISHC and ISCO schedules

N=1500 RPM, P_in=1.5 bar, and BMEP=5

4.4.2.1 FTIR emissions values:

An independent measurement of CO (Figure 4.10) by FTIR spectroscope reveals that the emission levels recorded by the two devices (E.S.A. emissions bench and FTIR) are in close agreement. The units here are parts per million (ppm).

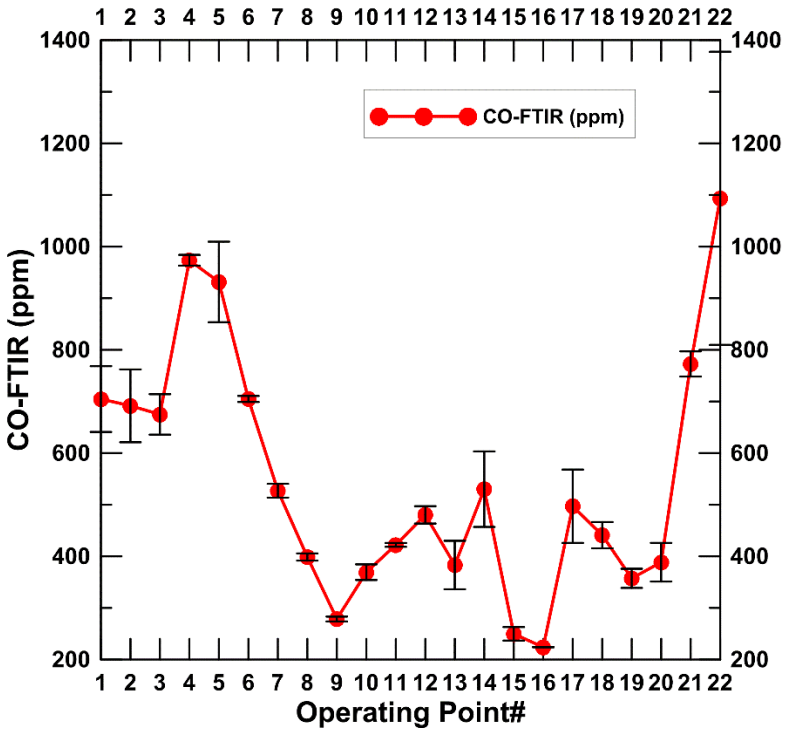

Figure 4.10 CO schedules-FTIR

N=1500 RPM, P_in=1.5 bar, and BMEP=5

4.4.3 Particle Concentrations and Sizes

The exhaust particle size and number concentrations are demonstrated in Figure 4.11 (a) and 4.11 (b). In general, the highest number of nanoparticles are in the diameter range of 8-15 nm. This is probably due the simpler molecular structure of methane, compared to diesel. The size of particles is bound by the lower detection limit of the EEPS device which is 6 nm. For single injection OP#1, a two spiked trend is observed while for all other OPs there is only one peak, which shows that a lot many particles of diameter 30-40 nm are produced with single injection strategy. The deployment of second injection limits the concentration of particles of size 30-40 nm. As evident from the figure, as the PES is decreased from 85 to 75, lower concentrations of nanoparticles

sized 15-100 nm diameter are formed. The least particle concentrations are shown by OP#6 and OP#7.

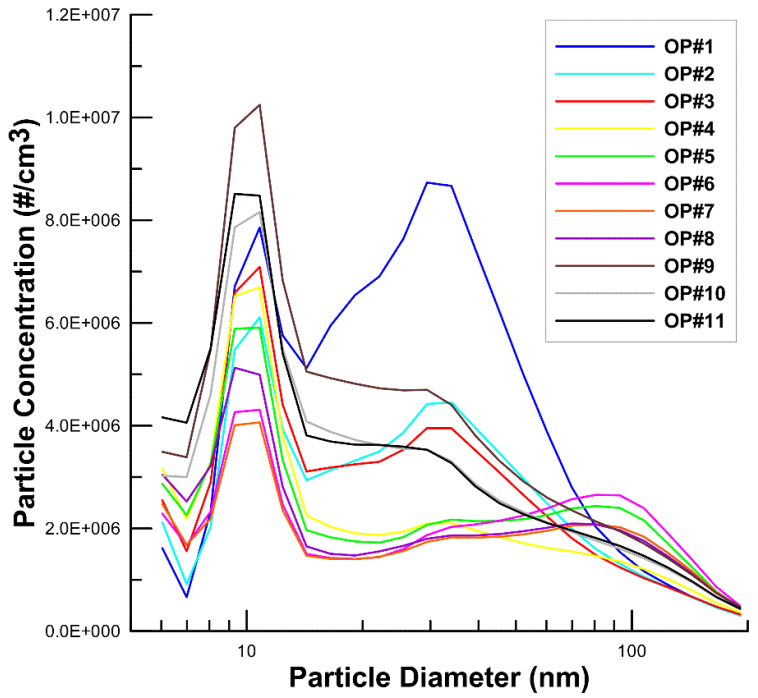

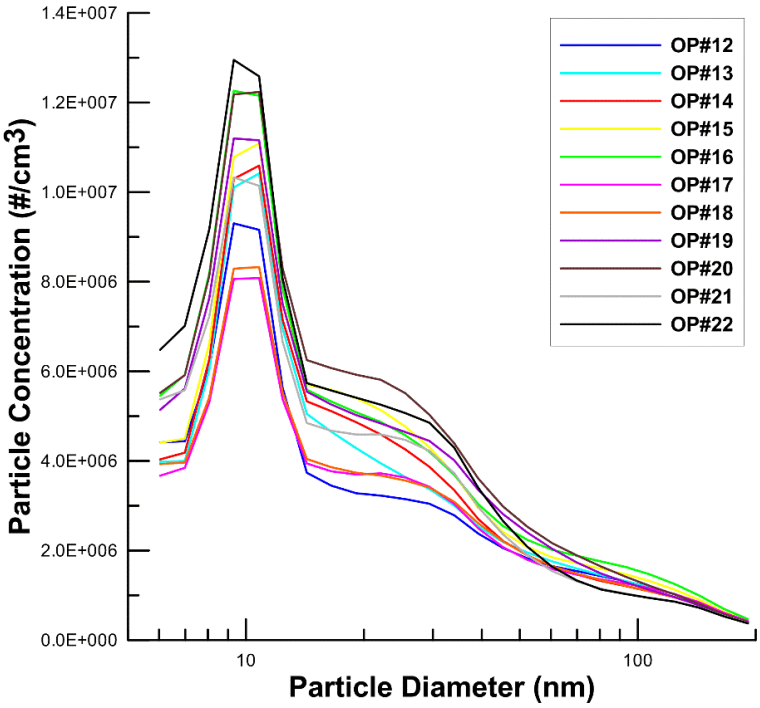

Figure 4.11 Particle size and their concentrations

(a): OP #1-11 at N=1500 RPM, P_in=1.5 bar, and BMEP=5
(b): OP #12-22 at N=1500 RPM, P_in=1.5 bar, and BMEP=5

CHAPTER V

CONCLUSION

Dual injection experiments with diesel pilot ignited methane dual fuel combustion were performed in an SCRE at constant engine speed and load of 1500 rpm and 5 bar BMEP, respectively, with no EGR. The first injection was held constant at 310 CAD while the second injection timing, rail pressure, PES were changed with the objective of reducing unburned hydrocarbons, CO, NOx and soot emissions.

1. Further separated secondary injection regimes (second inj. at 375 CAD) were more successful than close-coupled secondary injection regimes (second inj. at 320-325 CAD) in the simultaneous reduction of ISHC, ISCO and ISNOx emissions.
2. In-cylinder pressure, AHRR, combustion phasing (CA50) and IFCE are very sensitive to first pilot fuel injection duration.
3. Operating points with CA50 phasing closer to TDC have the highest fuel efficiencies.
4. ISNOx and ISHC have an inverse relationship with each other. One can be reduced at the expense of other merely by changing the injection durations of first & second injections.

5. Higher injection pressure generally lead to lower ISHC, ISCO, ISNOx and smoke emissions; but pilot injection duration has a more pronounced effect.

CHAPTER VI

RECOMMENDATION FOR FUTURE WORKS

1. The addition of an EGR would greatly enhance the range of experiments which can be performed on the SCRE. The current engine configuration is capable of withstanding loads until 7.5 bar BMEP, above which an EGR system would be required for operating within the MPRR limits of 10-12 bar/degree. It would also help in achieving even lower HC and CO emissions.
2. In the present study, effects of two diesel pilot injections were studied. Incorporating a third or even a fourth pilot injection could lead to interesting studies.
3. Additional levers, viz. higher intake boost (greater than 1.5 bar), higher air intake temperature could result in better HC and CO oxidation. Supposedly, this can increase the MPRR but given the fact that they remained fairly within limits of 12 bar/degree in this study, such levers could lead to positive outcomes.

REFERENCES

Abd Alla, G. H., Soliman, H. A., Badr, O. A., & Abd Rabbo, M. F. Effect of injection timing on the performance of a dual fuel engine. Energy conversion and Management 2002, 43(2), 269-277.

Abd Alla, G. H., Soliman, H. A., Badr, O. A., & Abd Rabbo, M. F. Effect of pilot fuel quantity on the performance of a dual fuel engine. Energy Conversion and Management 2000, 41(6), 559-572.

Alperstein, M., W. B. Swim, and P. H. Schweitzer. Fumigation Kills Smoke--Improves Diesel Performance. No. 580058. SAE Technical Paper, 1958.

Brunt, M., Rai, H., and Emtage, A. The Calculation of Heat Release Energy from Engine Cylinder Pressure Data 1998. SAE Technical Paper 981052.

Carlucci, A. P., et al. Experimental investigation and combustion analysis of a direct injection dual-fuel diesel–natural gas engine. Energy 33.2 (2008): 256-263.

Carlucci, A. P., et al. Improvements in Dual-Fuel Biodiesel-Producer Gas Combustion at Low Loads through Pilot Injection Splitting. Journal of Energy Engineering (2014).

Chen, Zhili, Mitsuru Konno, Mitsuharu Oguma, and Tadanori Yanai.Experimental study of CI natural-gas/DME homogeneous charge engine. No. 2000-01-0329. SAE Technical Paper, 2000.

Choi, Chang-Yong, and Rolf D. Reitz. An experimental study on the effects of oxygenated fuel blends and multiple injection strategies on DI diesel engine emissions. Fuel 78.11 (1999): 1303-1317.

Dec, J. E. (1997). A Conceptual Model of DI Diesel Combustion Based on Laser-Sheet Imaging. SAE Transactions, 106(3), 1319-1348.

Dec, J.E. “Diesel-Fueled HCCI Engines,” in Homogeneous Charge Compression Ignition (HCCI) Engines: Key Research and Development Issues Zhao, F. (Ed), SAE, Warrendale, PA, 2003.

Dec, John E. A conceptual model of DI diesel combustion based on laser-sheet imaging*. No. 970873. SAE technical paper, 1997.

Dec, John E., and Peter L. Kelly-Zion. The effects of injection timing and diluent addition on late-combustion soot burnout in a DI diesel engine based on simultaneous 2-D imaging of OH and soot. No. 2000-01-0238. SAE Technical Paper, 2000.

DieselNet. (2015), US EPA heavy-duty engine emissions standards, http://www.dieselnet.com/standards/us/hd.php, (accessed Feb. 28, 2015)

Dockery, D. P. (1994). Acute Respiratory Effects of Particulate Air Pollution. Annual Review of Public Health, 107-132.

Dwivedi, U. An experimental investigation of diesel-ignited gasoline and diesel ignited methane dual fuel concepts in a single cylinder research engine 2013, M.S. thesis, Mississippi State University. Ann Arbor: ProQuest/UMI. (Publication No. ETD 07032013-133320.)

E. S. Guerry, M.S. Raihan, A. Sohail, K. K. Srinivasan, S. R. Krishnan, Injection timing effects of diesel-ignited methane dual fuel combustion in a single cylinder research engine, Applied Energy (2014).

Flynn, P. F., et al. The inevitability of engine-out NO x emissions from spark-ignited and diesel engines. Proceedings of the Combustion Institute 28.1 (2000): 1211-1218.

Heywood, J.B., 1998, Internal Combustion Engine Fundamentals," McGraw Hill, Inc., ISBN 9-78-007028637-5:42-110.

Huestis, E., Erickson, P. A., & Musculus, M. P. (2007). In-cylinder and exhaust soot in low-temperature combustion using a wide-range of EGR in a heavy-duty diesel engine. SAE Technical Paper 2007-01-4017, doi: 10.4271/2007-01-4017

Jindal, S., et al. Experimental investigation of the effect of compression ratio and injection pressure in a direct injection diesel engine running on Jatropha methyl ester. Applied Thermal Engineering 30.5 (2010): 442-448.

Johnson, Timothy V, Diesel emissions in review, No. 2011-01-0304. SAE Technical Paper, 2011.

Kim, Myung Yoon, and Chang Sik Lee, Effect of a narrow fuel spray angle and a dual injection configuration on the improvement of exhaust emissions in a HCCI diesel engine, Fuel 86, no. 17 (2007) 2871-2880.

Krishnan, S. R., Biruduganti, M., Mo, Y., Bell, S. R., & Midkiff, K. C. Performance and heat release analysis of a pilot-ignited natural gas engine. International Journal of Engine Research 2002, 3(3), 171-184.

Lu, Xingcai, Junjun Ma, Libin Ji, and Zhen Huang. Simultaneous reduction of NOx emission and smoke opacity of biodiesel-fueled engines by port injection of ethanol. Fuel 87, no. 7 (2008): 1289-1296.

Ma, Zhihao, Zuohua Huang, Chongxiao Li, Xinbin Wang, and Haiyan Miao. Combustion and emission characteristics of a diesel engine fuelled with diesel–propane blends. Fuel 87, no. 8 (2008): 1711-1717.

Noguchi, Masaaki, et al. A study on gasoline engine combustion by observation of intermediate reactive products during combustion. No. 790840. SAE Technical Paper, 1979.

Northrop, William F., Stanislav V. Bohac, and Dennis N. Assanis. Premixed low temperature combustion of biodiesel and blends in a high speed compression ignition engine. No. 2009-01-0133. SAE Technical Paper, 2009.

Onishi, Shigeru, et al. Active thermo-atmosphere combustion (ATAC)-a new combustion process for internal combustion engines. No. 790501. SAE Technical paper, 1979.

Papagiannakis, R. G., Hountalas, D. T., & Rakopoulos, C. D. Theoretical study of the effects of pilot fuel quantity and its injection timing on the performance and emissions of a dual fuel diesel engine. Energy Conversion and Management 2007, 48(11), 2951-2961.

Particulates health risks (2015). Tesa clean air. http://www.tesa-clean-air.com/eng/fine_dust_particles (accessed March 11, 2015)

Plee, S., Ahmad, T., and Myers, J. (1981). Flame Temperature Correlation for the Effects of Exhaust Gas Recirculation on Diesel Particulate and NOx Emissions, SAE Technical Paper 811195, doi:10.4271/811195.

Polk, Andrew C., Chad D. Carpenter, E. Scott Guerry, Umang Dwivedi, Kalyan Kumar Srinivasan, Sundar Rajan Krishnan, and Zach L. Rowland. Diesel-ignited propane dual fuel low temperature combustion in a heavy-duty diesel engine. Journal of Engineering for Gas Turbines and Power 136, no. 9 (2014): 091509.

Qi, Y., K. K. Srinivasan, S. R. Krishnan, H. Yang, and K. C. Midkiff. Effect of hot exhaust gas recirculation on the performance and emissions of an advanced injection low pilot-ignited natural gas engine. International Journal of Engine Research 8, no. 3 (2007): 289-303.

Raihan, Mostafa S., et al. Experimental Analysis of Diesel-Ignited Methane Dual-Fuel Low-Temperature Combustion in a Single-Cylinder Diesel Engine. Journal of Energy Engineering (2014).

Ryu, K. Effects of pilot injection timing on the combustion and emissions characteristics in a diesel engine using biodiesel–CNG dual fuel. Applied Energy 2013a, 111, 721-730.

Saxena, S., and Bedoya, I. D., 2013. Fundamental phenomena affecting low temperature combustion and HCCI engines, high load limits and strategies for extending these limits. Progress in Energy and Combustion Science, 39(2013), 457-488.

Selim, M. Y. Sensitivity of dual fuel engine combustion and knocking limits to gaseous fuel composition. Energy Conversion and Management 2004, 45(3), 411-425.

Singh, S., Krishnan, S. R., Srinivasan, K. K., Midkiff, K. C., & Bell, S. R. Effect of pilot injection timing, pilot quantity and intake charge conditions on performance and emissions for an advanced low-pilot-ignited natural gas engine. International journal of Engine research 2004, 5(4), 329-348.

Sohail et al. Strategies for reduced UHC and CO emissions from Low Temperature Dual Fuel Natural Gas Combustion in a Single Cylinder Research Engine. Combustion Institute 2015.

Sorenson, Spencer C. Dimethyl ether in diesel engines: progress and perspectives. Journal of Engineering for Gas Turbines and Power 123, no. 3 (2001): 652-658.

Srinivasan, Kalyan K., Sundar R. Krishnan, Satbir Singh, K. Clark Midkiff, Stuart R. Bell, Weidong Gong, Scott B. Fiveland, and Martin Willi. "The advanced injection low pilot ignited natural gas engine: A combustion analysis."Journal of engineering for gas turbines and power 128, no. 1 (2006): 213-218.

Srinivasan, K. K., S. R. Krishnan, Y. Qi, K. C. MIDKIFF∗, and H. Yang. "Analysis of diesel pilot-ignited natural gas low-temperature combustion with hot exhaust gas recirculation." Combustion Science and Technology 179, no. 9 (2007): 1737-1776.

Stanglmaier, Rudolf H., and Charles E. Roberts. Homogeneous charge compression ignition (HCCI): benefits, compromises, and future engine applications. No. 1999-01-3682. SAE Technical Paper, 1999.

Stanglmaier, Rudolf H., Thomas W. Ryan, and Jason S. Souder. HCCI operation of a dual-fuel natural gas engine for improved fuel efficiency and ultra-low NOx emissions at low to moderate engine loads. No. 2001-01-1897. SAE Technical Paper, 2001.

U. S. Energy Information Administration, Monthly Energy Review – Table 1.3, February 2015, http://www.eia.gov/totalenergy (accessed Feb. 28, 2015).

U. S. Energy Information Administration, Monthly Natural Gas Gross Production Report, Feb 2015, http://www.eia.gov/oil_gas/natural_gas/data_publications/eia914/eia914.html (accessed Feb. 28, 2015)

Worldwide Emissions Regulations (2015), www.cumminsemissionsolutions.com (accessed Mar. 14, 2015)

APPENDIX A

SCRE LABVIEW CONTROLS

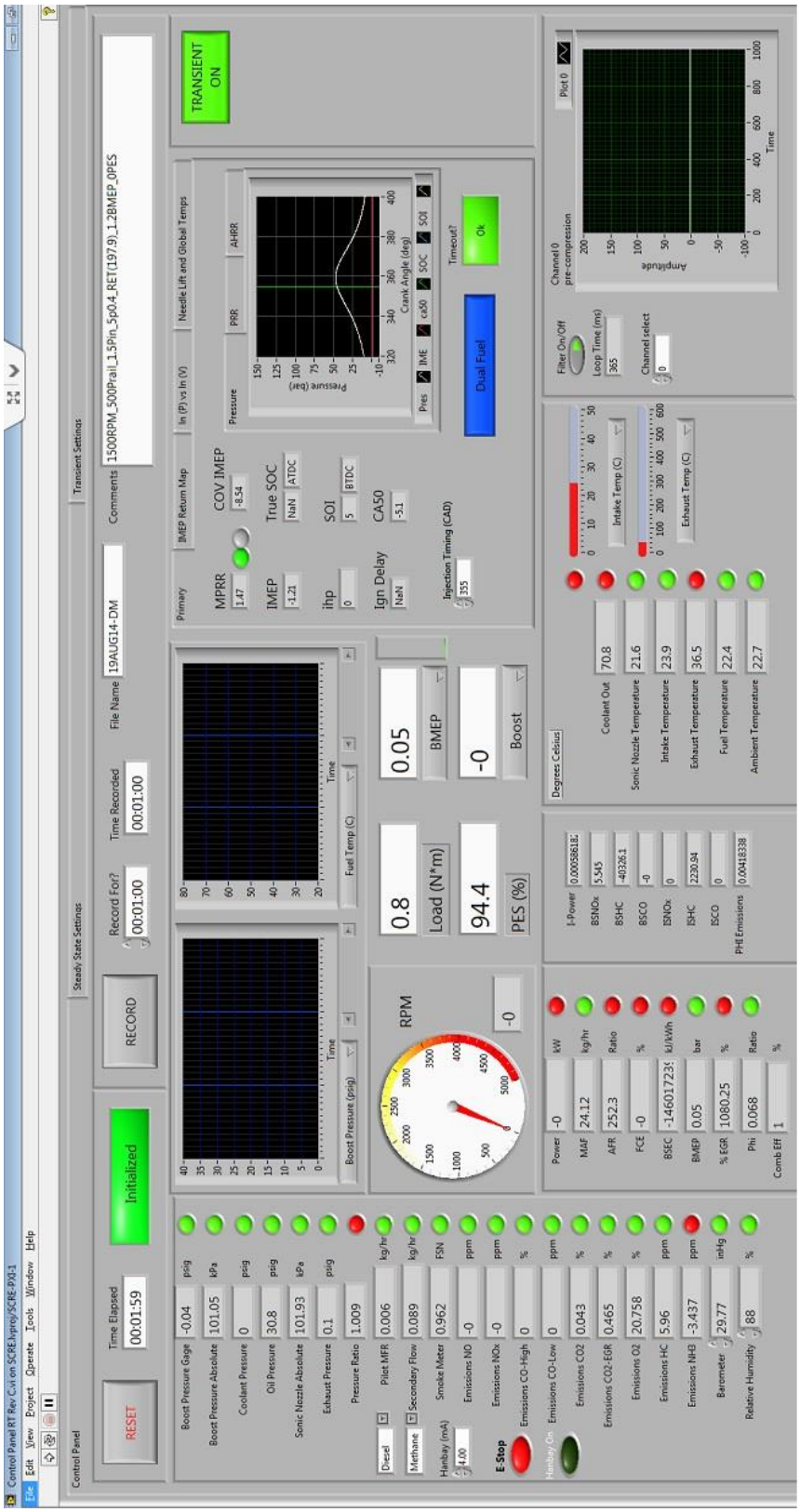

Figure A.1 Front Panel of LabVIEW controls on computer screen

APPENDIX B

E.S.A. EMISSIONS BENCH

The emissions bench is equipped with the following sampling trolley and analyzers:

B.1 Sampling Trolley

1. Primary filter
2. Heated line
3. Heated filter
4. ON/OFF switch
5. Grid to access the technical compartment

Figure B.1 Sampling trolley

The sampling trolley is specifically called as MICA 2M. It is used to sample, filter and condition motor exhaust gases directly from the engine test bed, then carry them towards an Engine Gases Analysis System (EGAS) to be analyzed. EGAS comprises the three analyzers: GRAPHITE 52M, TOPAZE 32M and MIR 2M. Thus, it enables measurement of total hydrocarbons (HCT), NO, NOx, CO, CO_2, and O_2.

MICA 2M normally consists of a fluid assembly which is heated and thermo-controlled at 191℃ ± 5℃. This assembly is composed of upstream heated lines (HL1-x) to sample motor exhaust gases, downstream heated lines (HL2) to transfer three gases

towards the EGAS, a heated pump to suck in and push out these gases and filters necessary to eliminate suspended particles. For this purpose, the HL1-x upstream lines are provided with a primary filter (porosity 2 μm) and the heated pump inlet equipped with a heated filter (porosity 1.2 μm).

MICA 2M is also equipped with a fluid circuit at ambient temperature dedicated to CO_2-EGR measurement. This EGR circuit consists of an independent pump, filters and a pressure controller.

MICA 2M is equipped with a fluid circuit under vacuum pressure, including a vacuum pump associated to TOPAZE 32M for NOx measurement, an activated charcoal filter to remove O_3, NO_2 and CO from gases before disposal through vent system. The independent control of pneumatic functions (pumps and solenoid valves) and the temperature control of heated lines, pump head and heated filters take place because of the specific electronics box of MICA 2M.

B.2 Flame Ionization Detector (FID): Unburnt HC detection

FID is the automotive emissions industry standard method of measuring hydrocarbon (HC) concentration. The setup for FID is housed inside GRAPHITE 52M trolley of the emissions bench.

Working Principle: The sample gas is introduced into a hydrogen-helium mixed flame inside the FID. Any hydrocarbons in the sample will produce ions when they are burnt. The ionization mechanism of organic substances in the flame is carried out in two phases:

1) Cracking of organic compounds in the central zone of the flame and generation of $CH^{\bullet}$, $CH_2^{\bullet}$,$CH_3^{\bullet}$ radicals

2) Chemical ionization in contact with oxygen according to the reaction:

$$CH^{\bullet} + O \rightarrow CHO^{+} + e^{-}$$

Ions are detected using a metal collector which is biased with a high DC voltage (polarization). The current across this collector is thus proportional to the rate of ionization which in turn depends upon the concentration of HC in the sample gas. This current is converted into voltage by an amplifier having a very high sensitivity (electrometer). The electric signal delivered is digitized in order to be processed by the microprocessor.

The FID detector gives a signal proportional to the carbon atoms number making up the hydrocarbon molecules present in the sample (total hydrocarbons). To carry out selective measurement of methane, the sample passes through an oven containing a catalyst in which temperature is adjusted for the C_2 to C_6 hydrocarbons conversion according to the reaction:

$$HC + O_2 \rightarrow CO_2 + H_2O$$

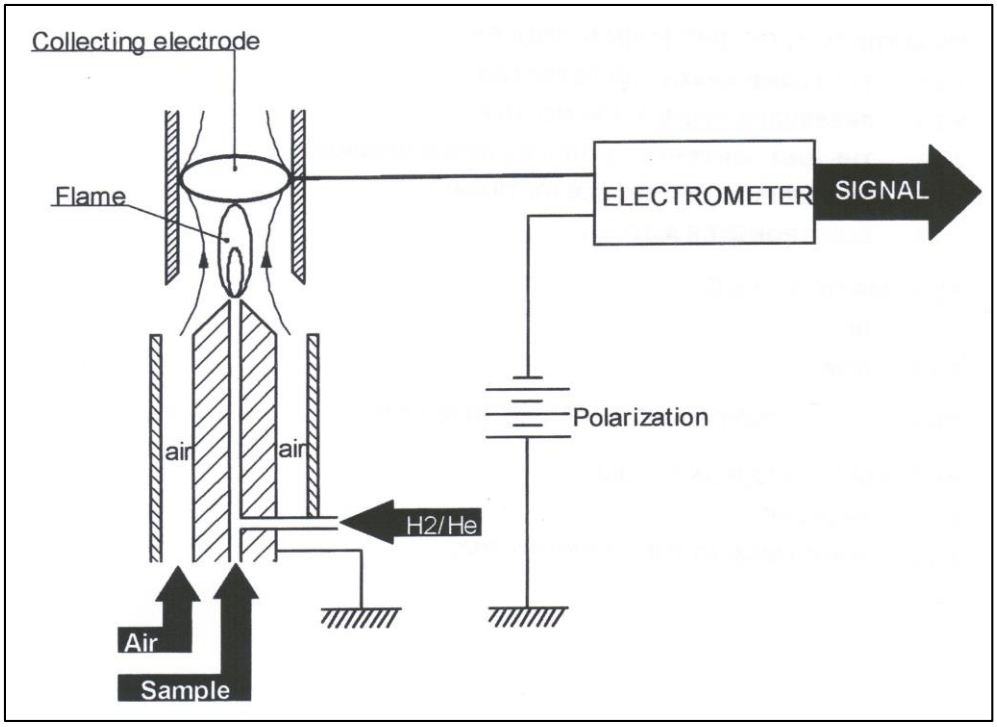

Figure B.2 Schematic of Flame Ionization Detector analyzer for detecting unburnt hydrocarbons

Source: Altech E.S.A. emissions bench operation manual

B.3 Chemiluminescence Detector (CLD): NO and NOx detection

CLD is the industry standard method of measuring nitric oxide (NO) concentration. The setup for CLD is housed inside TOPAZE 32M trolley of the emissions bench.

Working Principle: The reaction between NO and O3 (ozone) emits light. This reaction is the basis for the CLD in which the photons produced are detected by a photo multiplier tube. Chemiluminescence corresponds to the oxidation of NO molecules by ozone molecules:

$$NO + O_3 \rightarrow NO_2^{\bullet} + O_2$$

The return to a fundamental electronic state of the excited NO_2^* molecules is made by luminous radiation in a 600-1200 nanometers spectrum:

$$NO_2^* \rightarrow NO_2 + h\upsilon$$

The reaction chamber is separated from the detector by an optical filter, which selects only the radiation of wavelengths greater than 610 nanometers, thus eliminating interferences due to hydrocarbons. The radiation measurement is made by a photo-multiplier. The electrical signal delivered by the photo-multiplier is amplified and digitized for treatment by the microprocessor.

To be measured by chemiluminescence, NO_2 must be first transformed into NO. A carbon oven is used to carry out this reduction. Sampling is made by a pump located at the end of the circuit. The ozone necessary for the chemiluminescence reaction is generated by a discharge ozone generator.

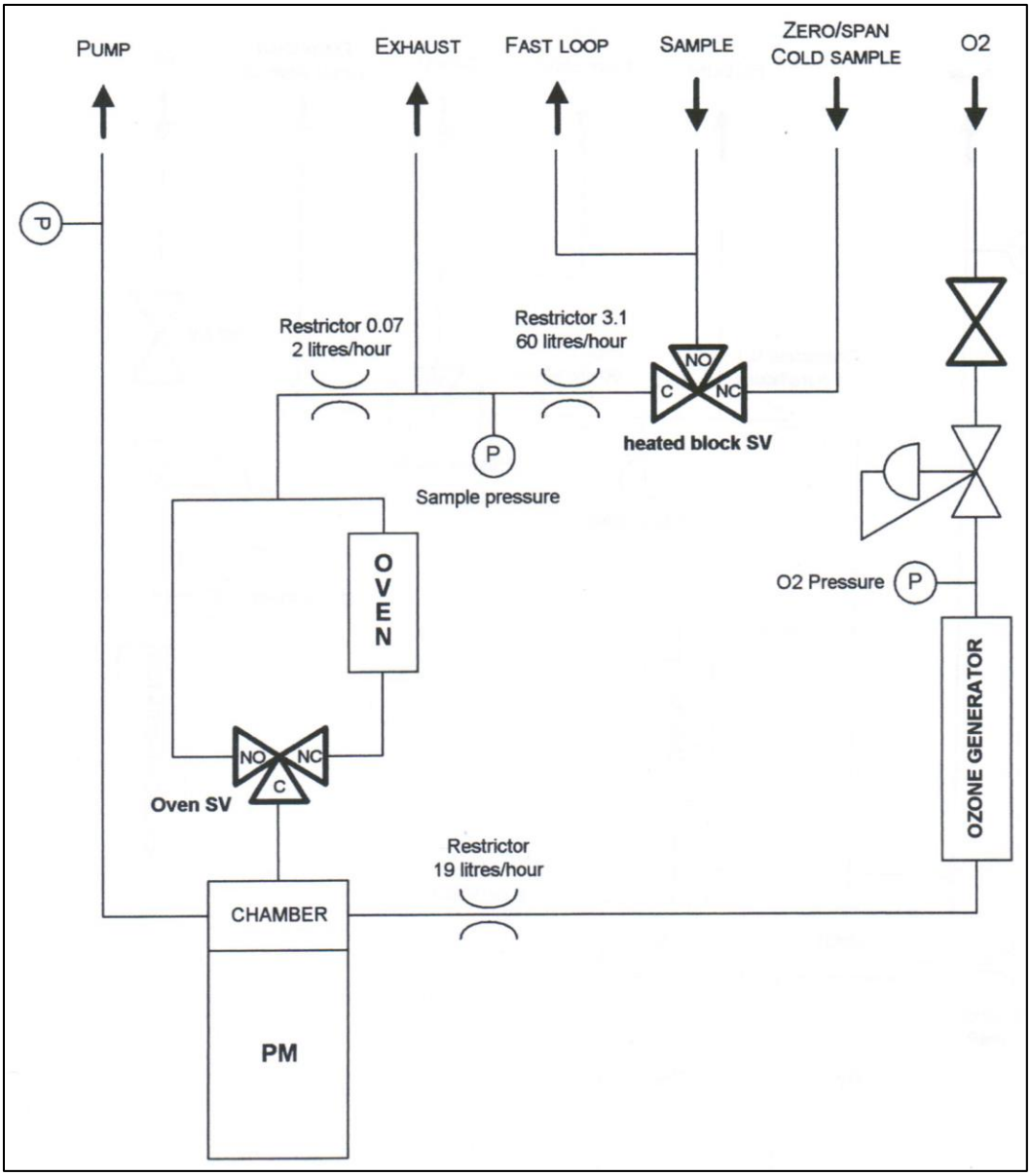

Figure B.3 Schematic of Chemiluminescence Detector for detecting NO and NOx

Source: Altech E.S.A. emissions bench operation manual

B.4 Non-Dispersive Infra-Red detector (NDIR):

NDIR detectors are the industry standard method of measuring the concentration of carbon oxides CO & CO2. The setup for NDIR is housed inside MIR 2M trolley of the emissions bench.

Working Principle: Each constituent gas in a sample will absorb some infra-red at a particular frequency. By shining an infra-red beam through a sample cell (containing CO or CO2), and measuring the amount of infra-red absorbed by the sample at the necessary wavelength, a NDIR detector is able to measure the volumetric concentration of CO or CO2 in the sample. A chopper wheel mounted in front of the detector continually corrects the offset and gain of the analyzer, and allows a single sampling head to measure the concentrations of two different gases.

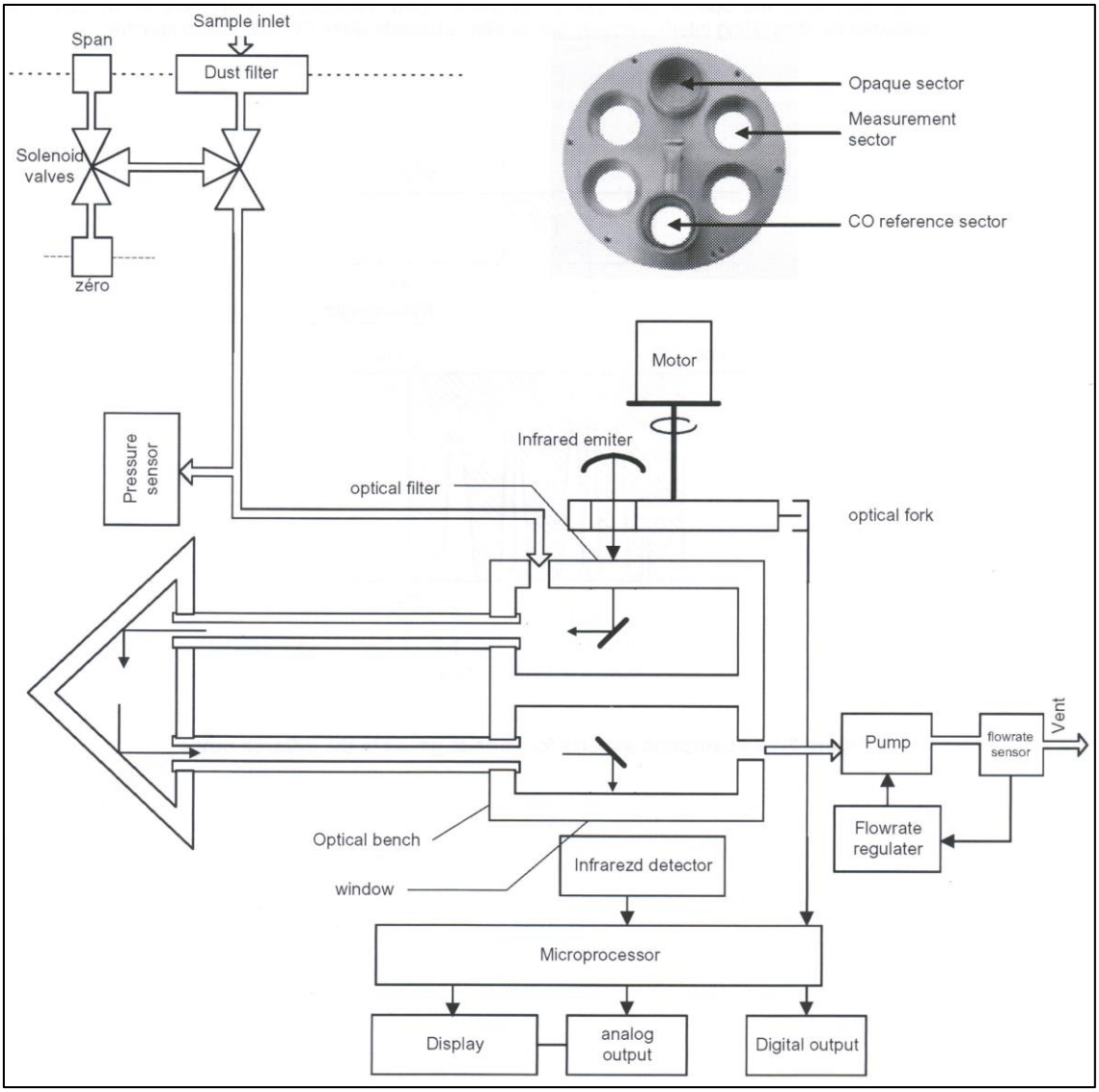

Figure B.4 Schematic of Non-Dispersive Infra-Red detector for detecting NO and NOx

Source: Altech E.S.A. emissions bench operation manual

B.5 Live emissions readings panel

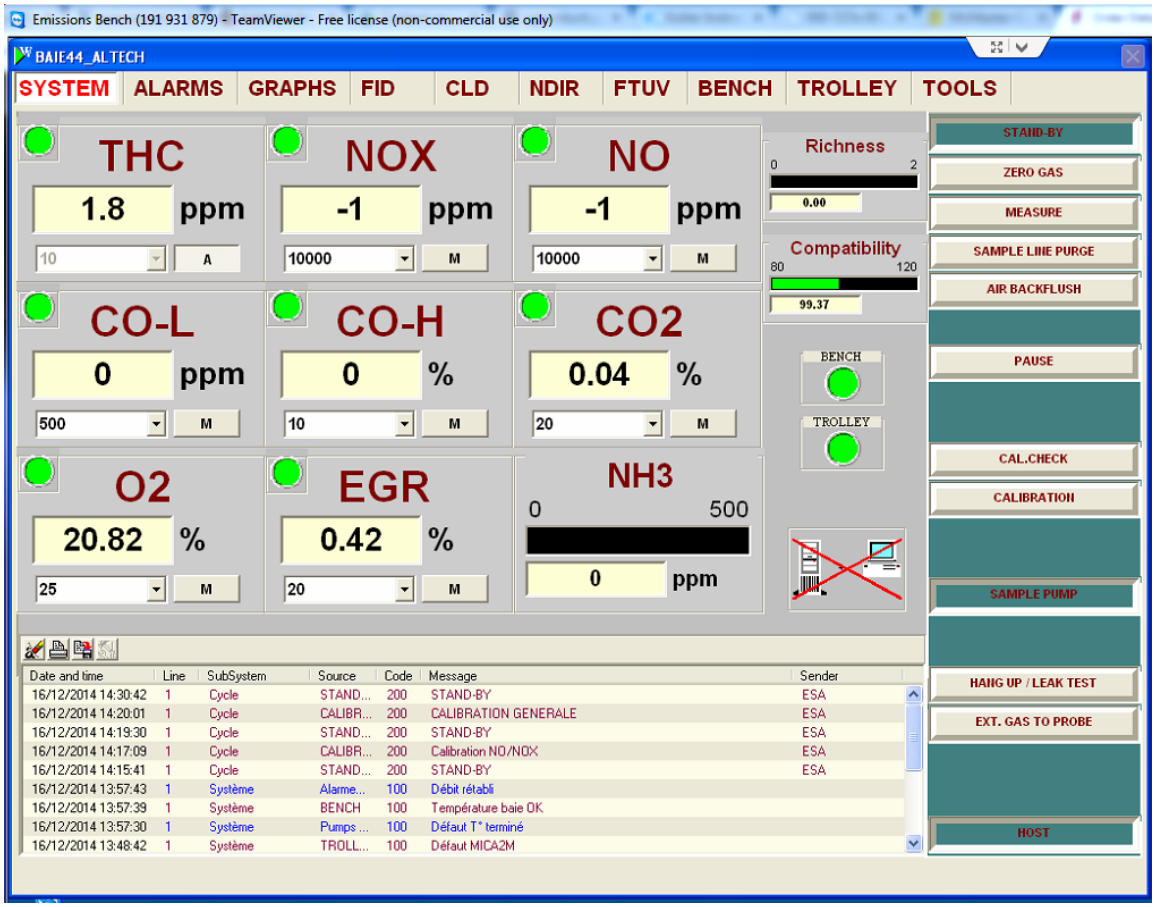

Figure B.5 Emissions readings panel

APPENDIX C

FTIR SPECTROSCOPE FOR EMISSIONS MEASUREMENT

C.1 Concept

FT-IR stands for Fourier Transform Infra-Red, the preferred method of infrared spectroscopy. In infrared spectroscopy, IR radiation is passed through a sample. Some of the infrared radiation is absorbed by the sample and some of it is passed through (transmitted). The resulting spectrum represents the molecular absorption and transmission, creating a molecular fingerprint of the sample. Like a fingerprint no two unique molecular structures produce the same infrared spectrum. This makes infrared spectroscopy useful for several types of analysis.

C.2 Working Principle

The FTIR measuring principle is a measurement with IR light. Contrary to NDIR with a narrow wave length area by means of an optical filter, the scan area of the IR wave length by use of the FTIR measuring principle is large. The principle of FTIR is that the gas to be analyzed is led through a cuvette with an IR light source at one end that is sending out scattered IR light, and a modulator that "cuts" the infra-red light into different wavelengths. At the other end of the cuvette, a detector is measuring the amount of IR light to pass through the cuvette. Like the NDIR measuring principle, it is the absorption of light at different wavelengths that is proportional to the concentration of gases to be analyzed. By data processing, Fourier Transformation mathematics is used to turn the measured absorption values into gas concentrations for the analyzed gases. As the light, when using the FTIR measuring principle, is modulated into different wavelengths, it is possible to analyze many different gases in the same instrument viz. CO, H_2O, NO, NOx, etc. As compared to conventional NDIR, use of this measurement

principle also produces a much larger data material from where the concentrations of the different gases can be measured.

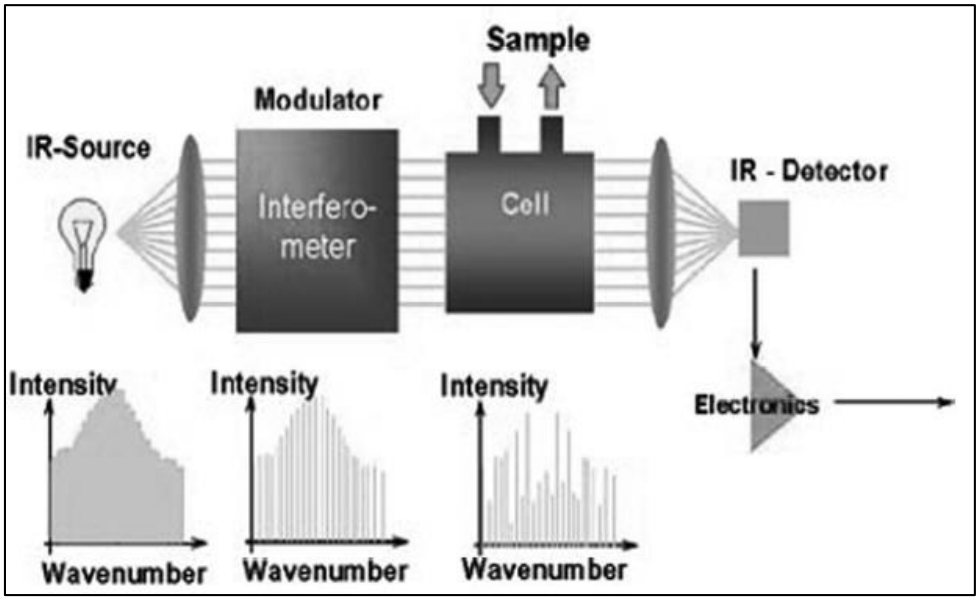

Figure C.1 Working principle of Fourier Transform Infra-Red spectroscope

Source: www.avl.com

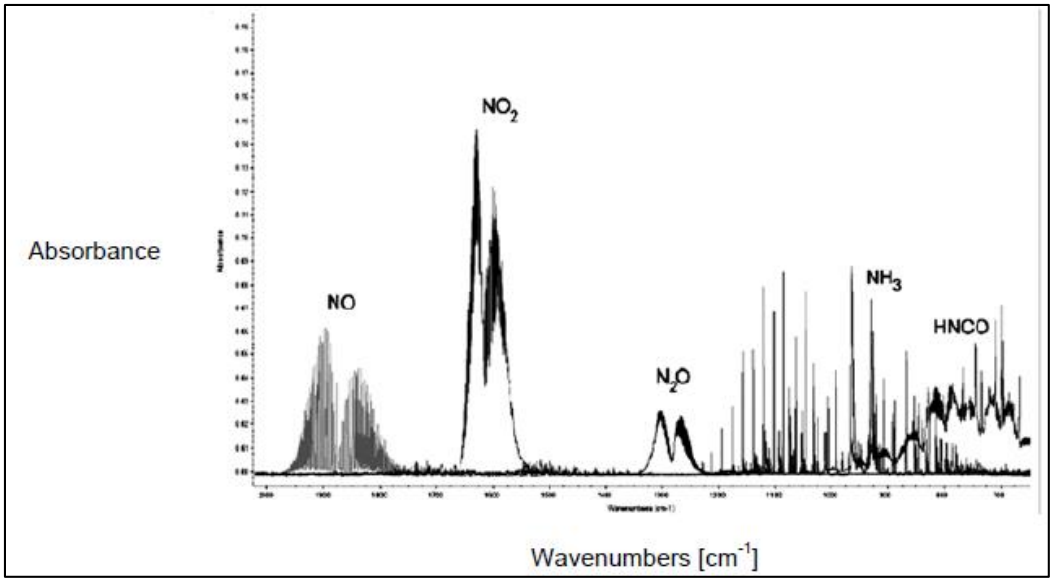

Figure C.2 Fourier Transform Infra-Red spectrum containing data of different gas species on x-axis and their relative absorbance on y-axis

Source: www.avl.com

C.3 Layout of components

The AVL SESAM-FTIR employed in this study uses a Michelson Interferometer with two mirrors, a fixed one and a movable one. The wideband infrared radiation of the light source is split into two beams by a beam splitter. One of the beams hits the fixed mirror and the other one hits the movable mirror. They are subsequently added to one beam. With the interference effects varying erasing and amplification of single wavelengths occur depending on the position of the movable mirror. This modified infra-red light is transferred into the gas cell. At each scan of the mirror, an interferogram (history of intensity over time) is registered by the infrared detector and reported in ppm levels after applying Fourier Transform. The values are shown in real-time during the engine transient conditions.

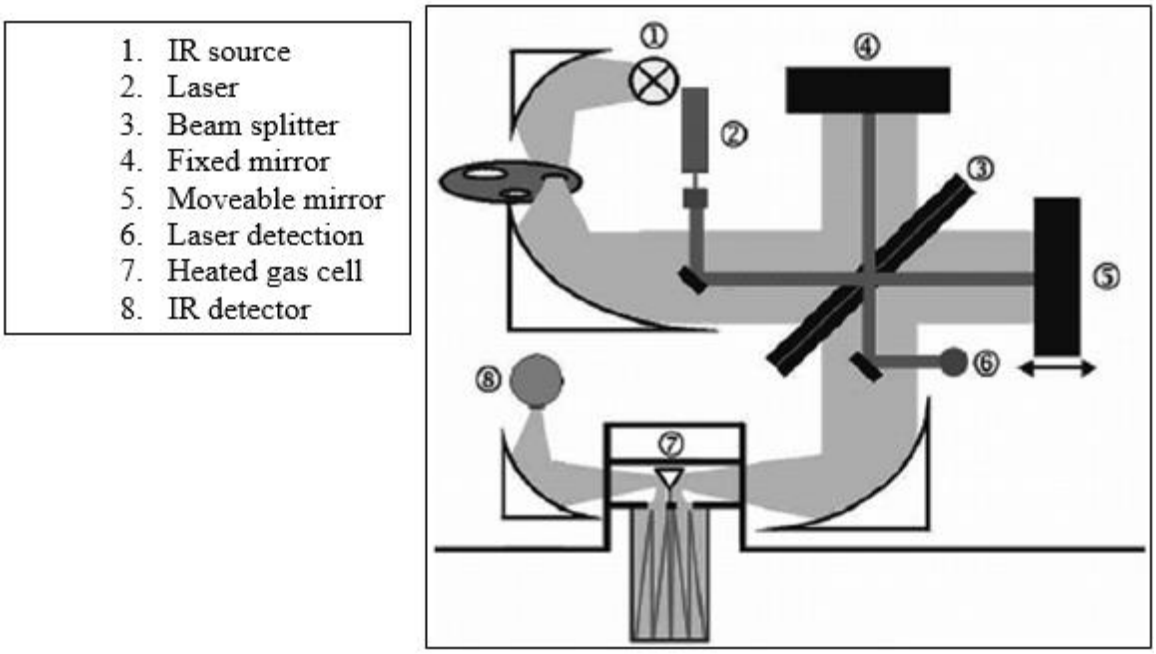

Figure C.3 Layout of Fourier Transform Infra-Red spectroscope components

Source: www.avl.com

APPENDIX D

EEPS ANALYZER

D.1 Concept

The Engine Exhaust Particle Sizer (EEPS) spectrometer is a fast-response, high-resolution instrument that measures very low particle number concentrations in diluted exhaust. It measures the size distribution and number concentration of engine exhaust particle emissions in the range from 5.6 to 560 nanometers, covering the entire range of interest.

Figure D.1 Engine Exhaust Particle Sizer

Source: www.tsi.com

D.2 Working Principle

The instrument draws a sample of the exhaust flow into the inlet continuously (Figure D.1). Particles are positively charged to a predictable level using a corona charger. Charged particles are then introduced to the measurement region near the center of a high-voltage electrode column and transported down the column surrounded by HEPA-filtered sheath air. A positive voltage is applied to the electrode and creates an electric field that repels the positively charged particles outward according to their electrical mobility.

Charged particles strike the respective electrometers and transfer their charge. A particle with higher electrical mobility strikes an electrometer near the top; whereas, a particle with lower electrical mobility strikes an electrometer lower in the stack. This multiple detector arrangement using highly sensitive electrometers allows for simultaneous concentration measurements of multiple particle sizes.

With a built-in, high-performance DSP, the Model 3090 uses a sophisticated, real-time data inversion to de-convolute data. As shown in Figure 3, the inversion accounts for variability in particle charge, image charge, multiple voltages on the center rod, and detection time to present a size distribution that corresponds to a specific time. The EEPS spectrometer provides the ability to measure particle emissions in real time.

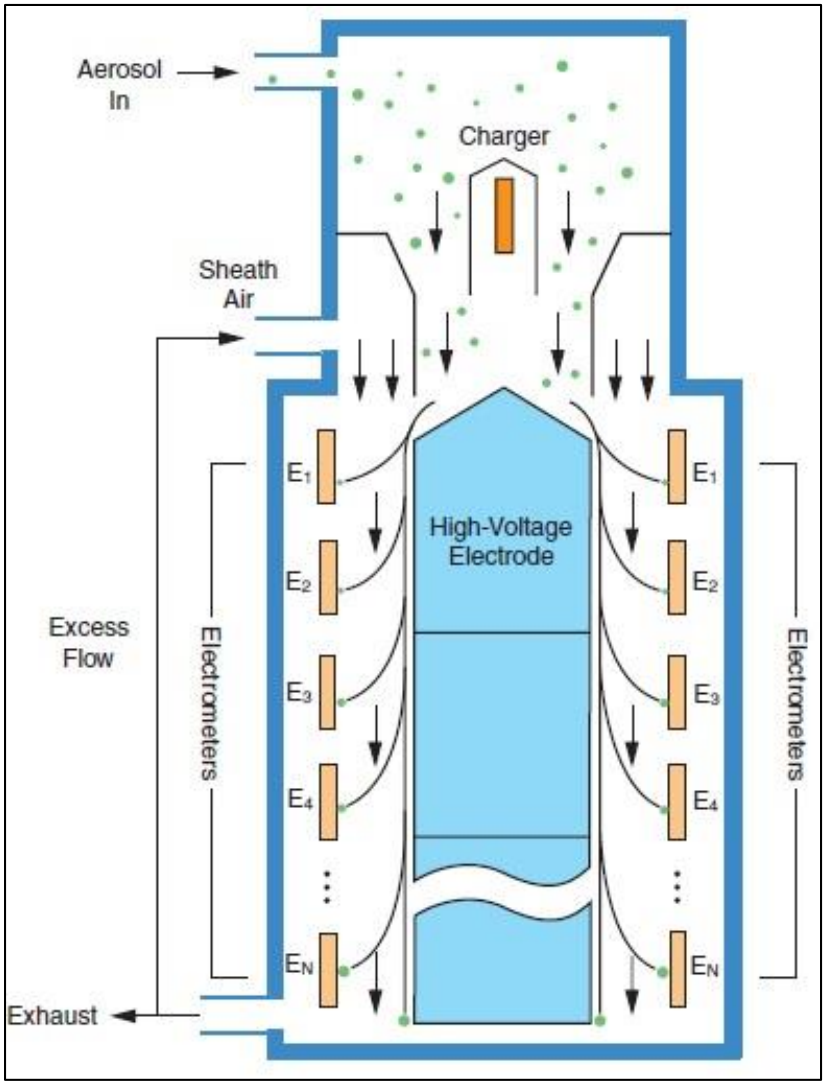

Figure D.2 Schematic of gas flow in Engine Exhaust Particle Sizer

Source: www.tsi.com

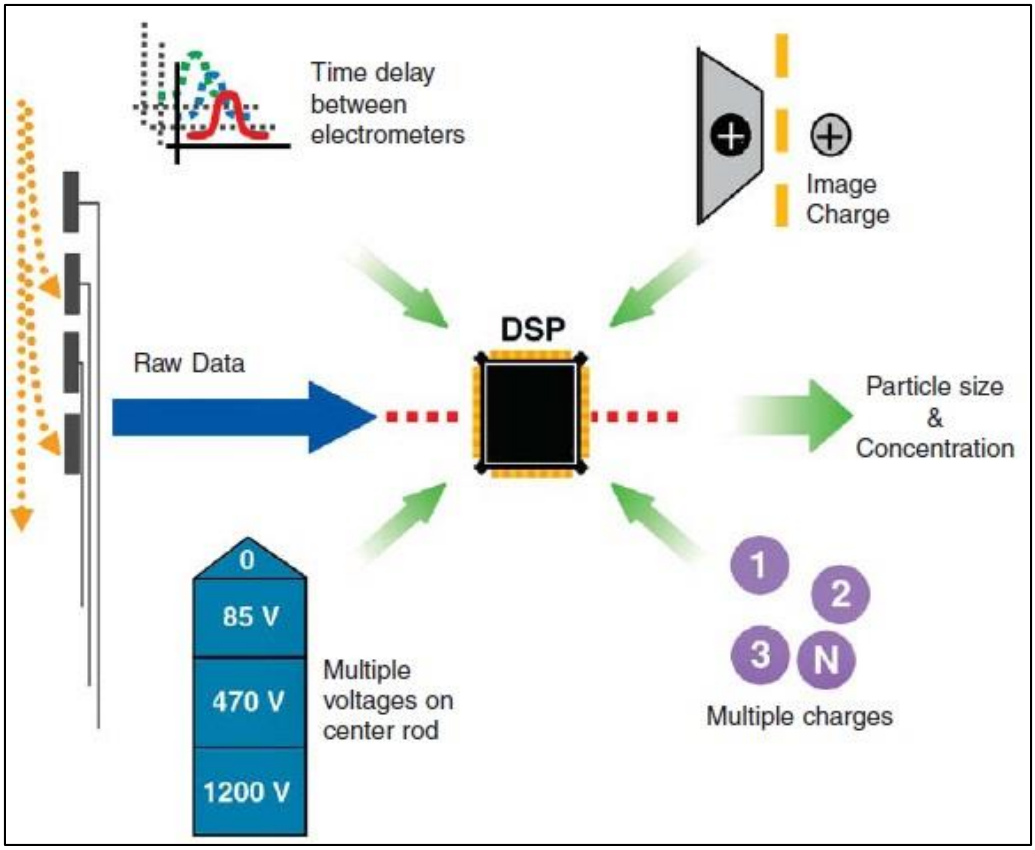

Figure D.3 Schematic of data inversion in Engine Exhaust Particle Sizer

Source: www.tsi.com

D.3 Front Panel

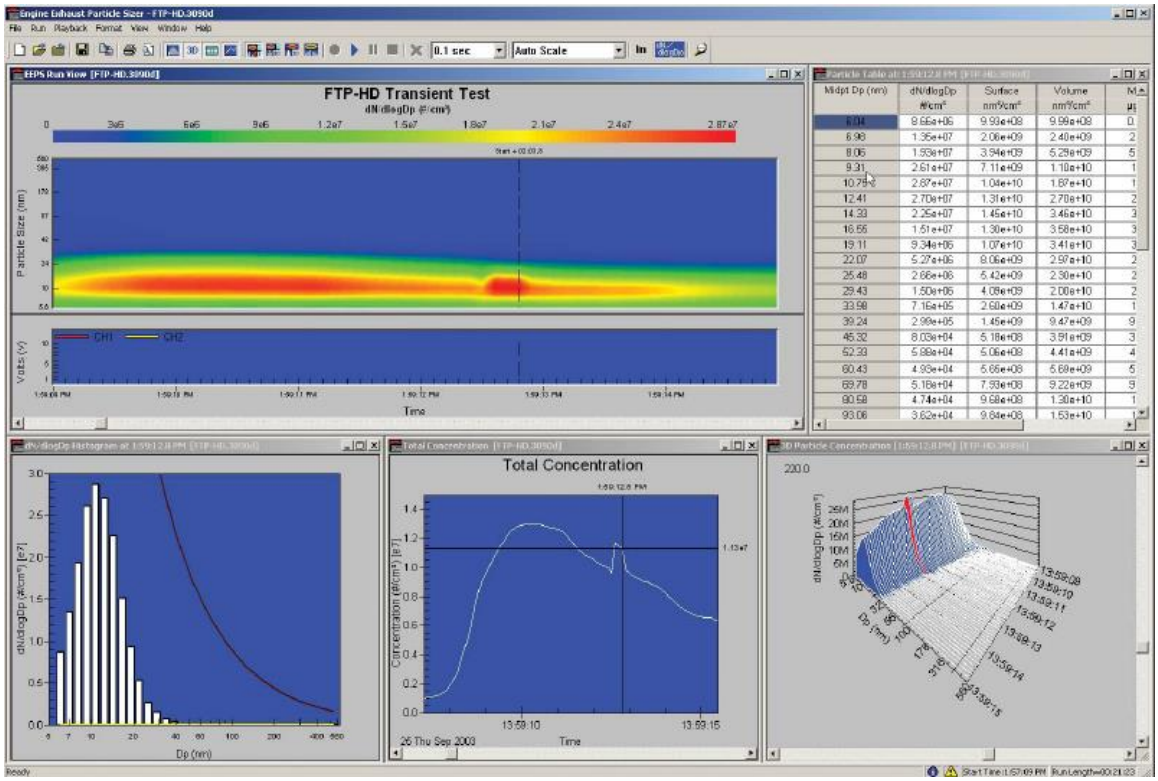

Figure D.4 Engine Exhaust Particle Sizer front panel on computer screen

APPENDIX E

SMOKEMETER

The smoke meter measures the smoke (also called Soot or Particulate Matter) levels in the engine exhaust gas. It is manufactured by AVL. It basically consists of a sampling tube, a reflectometer, filter paper roll, microprocessor and reading panel. The exhaust gas is taken from the exhaust using a probe and delivered to the smoke meter, wherein it is passed through a filter paper on which the soot gets deposited. This deposition causes a relative blackening of the filter paper which is read by the reflectometer using know standards for different blackening levels. The smoke is analyzed by the microprocessor and reported in unit-less Filter Smoke Numbers (FSN). An image of the smoke meter setup is shown below.

Figure E.1 AVL smoke meter

APPENDIX F

AIR FLOW MEASUREMENT

F.1 Sonic Flow Meter

The sonic flowmeter is a device to calculate the mass flow rate of the inlet air (Figure F.1). It works on the principle of achieving choked flow (Mach 1) at the throat of a converging-diverging nozzle (minimum cross-sectional area) while the upstream (P1 in the below Figure) and temperature are measured to give the mass flow according to the equation:

$$\text{Mass Flow} = \frac{A.P1}{\sqrt{T1}} * \sqrt{\frac{\gamma}{R}} * \left(\frac{\gamma+1}{2}\right)^{-\left[\frac{\gamma+1}{2(\gamma-1)}\right]}$$

Where: A = Cross-sectional area of the throat (minimum area)

P1 = Inlet pressure of the flowmeter

T1 = Inlet temperature of the flowmeter

γ = Specific heat ratio (C_p/C_v)

R = Universal gas constant

P3 = Outlet pressure of the flowmeter

The flowrate through the nozzle becomes a function of the inlet pressure, i.e. the doubling the inlet pressure doubles the flowrate. There is an increase in velocity and density as the gas accelerates through the flowmeter. The maximum air velocity is achieved at the throat where the cross-sectional area is the least and where the pressure ratio breaks Mach 1. Since the air consumption and required flowrate in the engine is dependent on the opening and closing cycles of its valves, there is a varying downstream air consumption. The sonic flowmeter has the advantage of maintaining the flowrate and upstream pressure from the air compressor even when there are pressure disturbances downstream. This is because the downstream pressure waves travelling at the speed of

sound cannot pass the throat which has the highest velocity (about Mach 1.2). And so they don't affect the velocity or density of the flow at the throat.

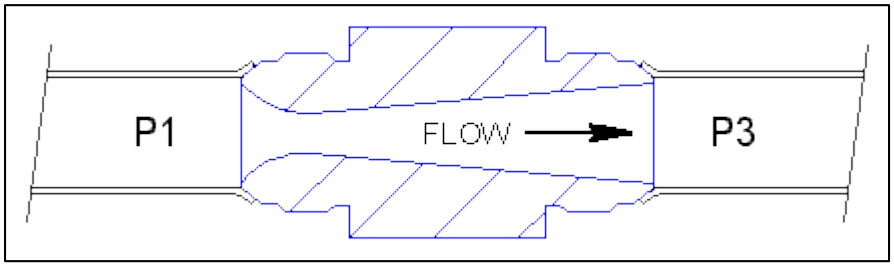

Figure F.1 Cross-section of the Sonic Flowmeter

Source: http://www.flowmaxx.com /sonic.htm

The setup uses a thermocouple, a pressure transducer and intake air from the air compressor. A schematic has been shown below (Figure F.2):

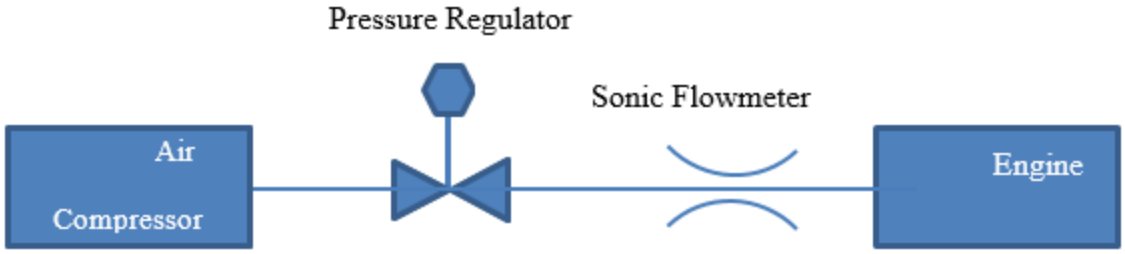

Figure F.2 Schematic showing the setup of the Sonic Flowmeter

APPENDIX G

FUEL FLOW MEASUREMENT

G.1 Coriolis Flowmeter

The Coriolis flowmeter measures the mass flow rate of the fuels (diesel and methane) flowing through tubes. A cross-sectional view of the device is shown in the Figure G.1. It is manufactured by Emerson Process Management. It consists of two parallel flow tubes (only one shown in the figure, the second tube being overlapped by the first tube) through which the fluid passes. The drive coil is energized, causing the two tubes to oscillate in the opposite direction to each other with their natural frequency. Due to the fluid momentum, the inlet legs of the flow tubes generate a Coriolis force that resists the vibration of the flow tubes. Similarly, as the mass flow moves through the outlet legs, the Coriolis force adds to the vibration of the flow tubes. It is the equal and opposite Coriolis force which results in a twisting motion of the tubes and is used to measure the mass flow rate through them. The pickoff coils convert this motion into a proportional voltage which is registered as a sine wave. The Resistance Thermal Device (RTD) reports the temperature of the passing fluid. Coriolis flowmeters are one of the most accurate flow rate measuring devices with the accuracy of 0.35% of reading for methane and 0.05% of reading for diesel. This level of accuracy is imperative to register the smallest change in the fuel efficiency. Moreover, the same model device has been used for measurement of both diesel and methane flow rates.

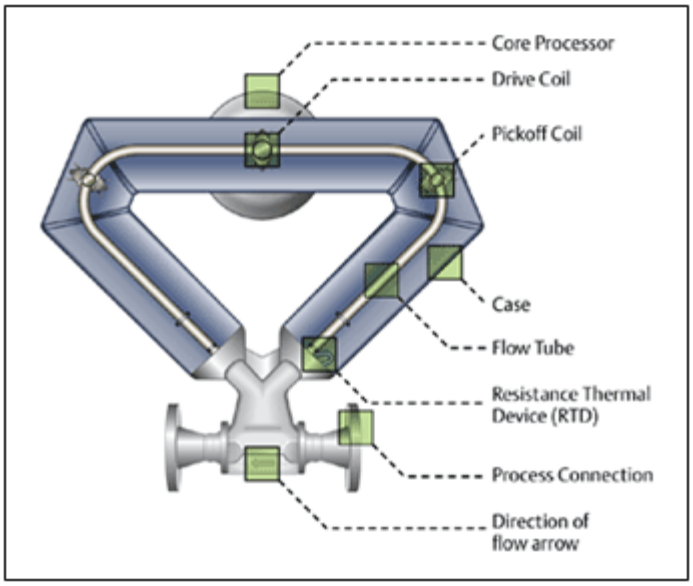

Front view

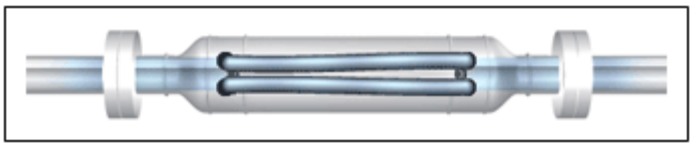

Top-view

Figure G.1 Schematic of the Coriolis Flowmeter

Source: http://www3.emersonprocess.com

The time delay between the inlet and the outlet sine waves is directly proportional to the mass flow rate through the pipe, i.e. greater the mass flow rate, greater the time delay (Figure G.2)

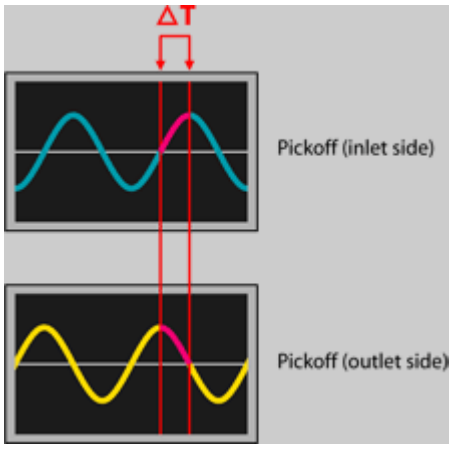

Figure G.2 Time-delay between the sine waves at the inlet and outlet of the flow tubes

Source: http://www3.emersonprocess.com